MASTERARBEIT | MASTER'S THESIS

Titel | Title

Earth as an Exoplanet: The Impact of Clouds on the Transmission Spectrum

verfasst von | submitted by

Isabella Winterer BSc

angestrebter akademischer Grad | in partial fulfilment of the requirements for the degree of

Master of Science (MSc)

Wien | Vienna, 2026

Studienkennzahl lt. Studienblatt | Degree programme code as it appears on the student record sheet:	UA 066 614
Studienrichtung lt. Studienblatt | Degree programme as it appears on the student record sheet:	Masterstudium Meteorology and Climate Science
Betreut von | Supervisor:	Univ.-Prof. Dr. Aiko Voigt

Abstract

This study investigates the impact of clouds, derived from simulations of the ICON-A climate model, on synthetic transmission spectra. To obtain a comprehensive overview, a parameter grid encompassing varying stellar sizes and orbital distances was analyzed. This approach allows for the evaluation of how different observational scenarios behave in relation to cloud coverage, utilizing realistic cloud simulations of Earth. The primary objective is to determine which geometric and stellar constellations are the most viable to target, particularly concerning the challenge of detecting water vapor (H_2O) and other key molecular signatures in the presence of clouds. The results demonstrate that, in addition to cloud masking, the planet-to-star radius ratio and atmospheric refraction play critical roles in signal detectability. The NIR H_2O, in particular, exhibits an exceptionally high signal loss when clouds are present. In an optimal observational scenario devoid of other limiting factors (such as atmospheric refraction or low astronomical contrast)—for instance, an Earth-like planet orbiting an ultra-cool M8 dwarf—clouds are found to dampen the H_2O transmission signal by up to 60%. In non-optimal scenarios—such as systems with larger host stars or wider orbits—this relative cloud-induced signal loss actually decreases. However, the overall detectability of atmospheric features in such systems drops significantly, as the absolute signal becomes severely limited by refraction and unfavorable star-to-planet area ratios.

Zusammenfassung

Diese Studie untersucht die Auswirkungen von Wolken, basierend auf Simulationen des ICON-A-Klimamodells, auf synthetische Transmissionsspektren. Um ein umfassendes Bild zu erhalten, wurde ein Parameterraster aus unterschiedlich großen Sternen und verschiedenen Bahndistanzen analysiert. Dieser Ansatz ermöglicht es, anhand realistischer Wolkensimulationen der Erde aufzuzeigen, wie sich verschiedene Szenarien in Bezug auf Wolkenbedeckung verhalten. Ziel ist es, zu ermitteln, welche Konstellationen für Beobachtungen am sinnvollsten sind, insbesondere im Hinblick auf die Erschwerung, Wasserdampf (H_2O) sowie weitere molekulare Signaturen bei vorhandenen Wolken nachzuweisen. Die Ergebnisse zeigen, dass neben der Wolkenmaskierung auch das Stern-zu-Planet-Radiusverhältnis und die atmosphärische Refraktion eine entscheidende Rolle für die Detektierbarkeit spielen. Besonders das NIR H_2O Band verzeichnet bei Vorkommen von Wolken einen extrem hohen Signalverlust. In einem optimalen Beobachtungsszenario ohne weitere Barrieren (wie Refraktion oder zu geringen astronomischen Kontrast) – also beispielsweise bei einem Planeten um einen M8-Zwerg – dämpfen die Wolken das H_2O-Signal um bis zu 60%. In weniger optimalen Szenarien – etwa bei größeren Sternen oder weiteren Umlaufbahnen – nimmt dieser relative, durch Wolken verursachte Signalverlust ab. Die generelle Detektierbarkeit atmosphärischer Merkmale sinkt in diesen Systemen jedoch drastisch, da Refraktion und ungünstige Stern-zu-Planet-Radiusverhältnisse das Signal limitieren.

Contents

1. Introduction

A planet's atmosphere serves as a crucial window into its climate, formation history, and potential habitability (Kreidberg, 2017). Most importantly, characterizing the atmospheric composition allows the search for biosignatures—trace gases such as oxygen, ozone, and methane, whose simultaneous presence in chemical disequilibrium may indicate the existence of a biosphere (Doshi et al., 2022; Macdonald & Cowan, 2019).

The most promising avenue for this atmospheric characterization is transmission spectroscopy, particularly with the advent of next-generation space observatories like the James Webb Space Telescope (JWST) (Barstow et al., 2015; Beichman et al., 2014). Currently, the most observationally accessible candidates for detecting these biosignatures are terrestrial, Earth-sized planets orbiting within the habitable zones of low-mass M-dwarf stars, such as the TRAPPIST-1 system (Fauchez et al., 2020; Pidhorodetska et al., 2020). Because of the small size and low luminosity of these host stars, their habitable zones are compact, and orbiting planets produce a much larger transit signal, making them the prime targets for near-term atmospheric characterization (Shields et al., 2016).

However, extracting these minute planetary signals from the overwhelming glare of the host star is immensely difficult. Even for these ideal M-dwarf targets, observations are strictly limited by complex geometric configurations and meteorological phenomena. To understand these limits, one must first consider how atmospheric signals are obtained.

1.1. Transmission Spectroscopy: Principles and Methodology

The observation of exoplanetary atmospheres is fundamentally a remote-sensing technique based on a stellar occultation measurement. In this geometry, the host star acts as a stable radiation source, and the planetary atmosphere serves as an attenuating medium as it passes across the stellar disk from the observer's perspective (Macdonald & Cowan, 2019).

The detection process follows three essential steps:

- Photon Counting: Modern space observatories, such as the James Webb Space Telescope (JWST), function as photon counters. These instruments utilize sensitive detectors (e.g., HgCdTe arrays) to collect starlight and convert individual incoming photons into measurable electronic signals (Beichman et al., 2014).
- Spectral Dispersion: To identify specific atmospheric constituents, the collected light is passed through a dispersive element, such as a prism or a diffraction grating. This separates the light into its constituent wavelengths, allowing the detector to record the intensity of each "color" individually. The presence of molecules like CO_2 or H_2O results in a wavelength-dependent reduction in the observed stellar flux (Brown, 2001; Seager & Sasselov, 2000).
- Statistical Precision: Because light is detected as discrete photons, the measurements are subject to inherent statistical fluctuations known as shot noise. This uncertainty is

governed by Poisson statistics, in which the precision of the signal scales with the square root of the number of detected photons. Consequently, for small, Earth-like planets with thin atmospheres, it is often necessary to average the data from multiple transit events to achieve a sufficient signal-to-noise ratio (Kreidberg, 2017; Seager & Mallen-Ornelas, 2003).

Transmission spectroscopy, as shown in figure 1, is a technique for probing the atmospheres of exoplanets as they pass in front of their host stars. During transit, a fraction of the starlight is absorbed or scattered by the planet's atmosphere. This leads to wavelength-dependent variations in the observed stellar flux.
To derive physical properties from the recorded photon flux, the geometric configuration of the planet-star system must be considered. In a transiting system, the most critical event for atmospheric characterization is the primary transit, which occurs when the planet passes directly between the observer and the host star (Seager & Mallen-Ornelas, 2003). The fundamental observable during a transit is the transit depth (ΔF), which represents the fraction of stellar light blocked by the planet. For a solid body without an atmosphere, this depth is simply the ratio of the projected areas of the planet (R_p) and the star (R_*):

$$\Delta F = \left(\frac{R_p}{R_*}\right)^2 \tag{1.1}$$

However, when a planet possesses an atmosphere, the situation changes. As starlight passes through the thin atmospheric ring (the limb), it is attenuated by absorption and scattering. This leads to the key concept of a wavelength-dependent radius: at wavelengths where the atmosphere is highly opaque (e.g., due to strong CO_2 absorption), the atmosphere blocks more light, making the planet appear larger to the observer (Brown, 2001). Consequently, the effective radius of the planet becomes a function of wavelength. For an atmosphere with absorbing and scattering molecules, the effective radius of the planet varies as a function of wavelength, modifying the transit depth as follows:

$$\Delta F(\lambda) = \left(\frac{R_p + h(\lambda)}{R_*}\right)^2 \tag{1.2}$$

where $h(\lambda)$ represents the altitude at which the atmosphere becomes optically thick at a given wavelength (Brown, 2001).

1.2. Observational Techniques and Challenges

The characterization of an exoplanetary atmosphere during a transit fundamentally depends on the measurement of spectral contrast, which quantifies the relative decrease in stellar flux as the planet's atmosphere attenuates the light of the host star. This contrast, $C(\lambda)$ is typically defined as the difference between the out-of-transit flux (F_{out}) and the in-transit flux (F_{in}), normalized by the stellar background (Villanueva et al., 2022):

$$C(\lambda) = 10^6 \times \left(\frac{F_{out}(\lambda) - F_{in}(\lambda)}{F_{out}(\lambda)}\right) \tag{1.3}$$

$C(\lambda)$ serves as the observational counterpart to $\Delta F(\lambda)$. It translates the geometric light attenuation into parts per million (ppm), providing the measurable unit for evaluating telescopic data. The resulting variation in transit depth can be approximated from Equation 1.3 by considering $h(\lambda)$, leading to the relation:

$$C(\lambda) \approx 10^6 \times \frac{h(\lambda)^2}{R_*^2} \tag{1.4}$$

Rather than the total transit depth, this contrast isolates the atmospheric contribution and quantifies the wavelength-dependent variation in the attenuated starlight. This equation highlights the critical role of R_* in determining the baseline signal (Villanueva et al., 2022). However, the achievable signal-to-noise ratio (SNR) is not a function of geometry but is also limited by the number of observed transits (N). Following Poisson statistics, the precision of the photon counting process improves with the square root of the number of events:

$$SNR \propto \sqrt{N}, \tag{1.5}$$

where N is the number of co-added transit events (Lustig-Yaeger et al., 2019). While next-generation instruments such as the James Webb Space Telescope (JWST) offer unprecedented opportunities for high-precision spectroscopy (Beichman et al., 2014; Fauchez et al., 2020), the intrinsic signal amplitude set by the star-planet ratio remains a decisive factor in the ultimate detectability of terrestrial atmospheres (Cowan et al., 2015; Doshi et al., 2022; Suissa et al., 2020). This statistical requirement means that for small planets, dozens of transits may be necessary to resolve key molecular features (Fauchez et al., 2019). Even with high statistical precision, the true atmospheric contrast is oftentimes suppressed. Barstow et al., 2015 note that stellar inhomogeneities, like star spots, can distort the measured contrast, while clouds and hazes act as a "gray" opacity source that mutes the amplitude of spectral lines (Cowan et al., 2015; Fauchez et al., 2019; Komacek et al., 2020). These limiting factors imply that the theoretical contrast is often a best-case scenario that is rarely met in realistic observational environments.

1.2.1. The Astronomic Barrier: Star-to-planet ratio

The most fundamental obstacle in characterizing terrestrial exoplanetary atmospheres by transmission spectroscopy is the overwhelming brightness of the host star relative to the minute signal of the planetary limb. As established in Seager and Mallen-Ornelas, 2003, this relationship is critical for deriving the physical parameters of the planet-star system. For Earth-sized planets orbiting Sun-like stars, the atmospheric contribution to this dimming typically occurs on the order of 1–10 ppm (Beichman et al., 2014; Misra et al., 2014). Such signals are often buried within stellar noise or instrumental systematics, making the detection of Earth-analogs around G-type stars a significant challenge (Suissa et al., 2020).
The fundamental challenge of transmission spectroscopy lies in the geometric and physical scaling of the observable signal. During a transit, the baseline stellar dimming is dictated by the planet-to-star area ratio (Seager & Deming, 2010). However, the atmospheric contribution to this signal—the actual transmission spectrum—is only a minute fraction of this transit depth and scales directly with the atmospheric scale height (Kreidberg, 2017). Hot Jupiters represent ideal targets because their high equilibrium temperatures, low surface gravities, and light, hydrogen-dominated atmospheres result in extensively inflated scale heights (Kreidberg, 2017). In stark contrast, terrestrial planets possess much lower temperatures, higher surface gravities, and heavier secondary atmospheres, which compress their scale heights into a very thin annulus (Seager & Deming, 2010).

The difficulty of detecting these signals is compounded by the planet-to-star flux ratio, which determines the intrinsic signal amplitude and effectively dilutes the planetary signatures. This relationship is described in Equation 1.2. While the amplitudes of spectral features for ideal targets like hot Jupiters are already small, the expected signals for Earth-like planets are two to three orders of magnitude smaller (Kreidberg, 2017). Such minute planetary signatures fall well below the 10^{-4} precision barriers of current instrumentation (Cowan et al., 2015). Consequently, the spectral features of the planet appear only as minor modulations within the dominant stellar spectrum (Wunderlich et al., 2019), making transmission spectroscopy a vital yet demanding diagnostic tool for atmospheric studies (Seager & Deming, 2010).
To mitigate this geometric suppression, modern observational strategies prioritize M-dwarf host stars. Their significantly smaller radii—specifically those characterized by $R_* < 0.33R_\odot$, where $R_\odot$ denotes the solar radius (Nutzman & Charbonneau, 2008)—provide a more favorable R_p/R_* ratio, which enhances the spectral contrast and facilitates the identification of molecular features (Gould et al., 2003).

1.2.2. The Geometric Barrier: Atmospheric Refraction

Atmospheric refraction represents a fundamental physical boundary for smaller planets like Earth. For these worlds, it imposes a strict limit on the depths that can be probed via transmission spectroscopy, acting as a refractive floor that is independent of cloud cover or aerosol opacity (Alp & Demory, 2018). During a primary transit, starlight passing through the planetary limb is bent due to vertical gradients in the atmospheric refractive index. This deflection can redirect light rays away from the observer's line of sight, effectively obscuring the lower atmosphere even in the absence of clouds (Betremieux & Kaltenegger, 2014; Sidis & Sari, 2010).
The accessibility of the lower atmosphere is determined by the angular size of the host star as seen from the planet. A light ray can only reach the observer if its total deflection is less than the stellar angular semi-diameter. Betremieux and Kaltenegger, 2014 provides a detailed analytical treatment of this limit, deriving a relationship for the maximum observable pressure, p_{max}:

$$\frac{p_{max}}{p_0} = \frac{1}{\nu_0} \frac{R_* + R_p}{a} \sqrt{\frac{H}{2\pi R_p}} \tag{1.6}$$

where p_0 is the surface pressure, ν_0 is the atmospheric refractivity, a is the orbital distance, R_* and R_p are the stellar and planetary radii, and H is the scale height. In essence, Equation 1.6 determines the critical altitude by equating the optical bending power of the planetary atmosphere to the geometric viewing angle of the system. The term $\frac{R_*+R_p}{a}$ approximates the angular size of the host star as seen from the exoplanet. For a refracted light ray to reach a distant observer during transit, its total deflection cannot exceed this angular extent. The remaining terms describe the atmosphere's capacity to bend that light. The refractivity ν_0 dictates the intrinsic optical bending power of the gas mixture, while the factor $\sqrt{\frac{H}{2\pi R_p}}$ accounts for the path length of the light ray through the spherical, exponentially decaying atmosphere (Betremieux & Kaltenegger, 2014).
Because atmospheric density—and thus the refractive index—increases exponentially with depth, light rays penetrating deeper into the atmosphere experience drastically stronger deflection. Consequently, p_{max} defines the exact pressure level where the atmospheric deflection perfectly matches the star's angular extent. Any light rays passing below this critical boundary

are bent so severely that they miss the observer entirely, rendering the lower atmosphere inherently invisible regardless of cloud coverage or atmospheric opacity (Betremieux & Kaltenegger, 2014).

As further detailed by Alp and Demory, 2018, the refractivity ν_0 is highly dependent on the chemical composition of the atmosphere, with different gasses such as N_2, O_2, and CO_2 exhibiting unique refractive and dispersive properties (defined by Cauchy's equation).

This relationship illustrates that p_{max} is extremely sensitive to the star-planet separation (a). For an Earth-Sun analog, the small angular size of the Sun results in a high refractive floor at approximately $p_{max} \approx 0.24$ bar, masking the atmosphere below 12.6 km (Betremieux & Kaltenegger, 2014; Macdonald & Cowan, 2019). This effectively hides the majority of the troposphere, including critical transparency windows.

In contrast, planets in the habitable zones of M-dwarfs are positioned significantly closer to their host stars. This closer proximity increases the angular size of the stellar disk, allowing the system to tolerate much larger refractive deflections. As demonstrated by Misra et al., 2014, the refractive floor for Earth-sized planets orbiting late M-dwarfs often lies at or near the planetary surface ($\sim$1 bar). Consequently, M-dwarf systems provide a unique geometric window to probe the near-surface environment where biosignatures are most concentrated—a task that remains physically impossible for Earth-analogs orbiting G-type stars (Betremieux & Kaltenegger, 2014; Macdonald & Cowan, 2019).

The interplay between refraction and stellar type creates a significant selection bias in atmospheric characterization. Refraction sets the ultimate hard limit for the detectable signal. With instruments like the JWST, the intrinsic signal amplitude of terrestrial atmospheres remains a decisive factor, often requiring the co-addition of dozens of transits to overcome the dilution of spectral features caused by these combined geometric and meteorological barriers (Fauchez et al., 2022; Moran et al., 2018; Pidhorodetska et al., 2020).

1.2.3. The Meteorological Barrier: Cloud Opacity and Vertical Masking

For terrestrial exoplanets, the distribution and optical thickness of clouds play a defining role in atmospheric observability. The presence and vertical distribution of clouds are among the most critical factors limiting the observability of molecular features in exoplanet transmission spectra. Clouds act as a non-selective gray opacity source that raises the apparent continuum of the planet across a wide wavelength range, thereby masking molecular absorption features in the lower atmosphere (Komacek et al., 2020). This vertical filtering effect creates a fundamental observational challenge: while a "clear-sky" scenario allows for deep probing of the atmospheric composition, the presence of an opaque cloud deck can effectively truncate the transmission spectrum and mute the signal of key absorbers such as H_2O, CH_4, and O_3 (Suissa et al., 2020; Wunderlich et al., 2019).

The severity of this masking is primarily governed by the clouds' vertical distribution and altitude. High-altitude clouds, particularly those reaching the upper troposphere or lower stratosphere, obscure the deeper, high-pressure regions where molecular concentrations are typically highest. While well-mixed species like CO_2 might be identified in fewer than five transits, the detection of biosignatures like O_3 or CH_4 can require upwards of 80 transits under realistic, cloudy conditions (Macdonald & Cowan, 2019).

It is crucial to distinguish between the cloud properties of true Earth analogs and those of tidally locked M-dwarf planets. As demonstrated by Doshi et al., 2022 using empirical solar occultation data, high-altitude stratospheric clouds on Earth are optically thin and only alter

the transmission spectrum by a maximum of 10–15 ppm, meaning they do not significantly impede JWST observations. In stark contrast, 3D General Circulation Models for tidally locked aquaplanets orbiting M-dwarfs show that strong dayside convection transports massive amounts of moisture to high altitudes, creating optically thick and extensive cloud decks at the terminator (Suissa et al., 2020). These extreme, continuous cloud layers mute spectral features far more severely than the fragmented, thin cirrus clouds of modern Earth (Doshi et al., 2022). Recent three-dimensional climate models of terrestrial exoplanets reveal that the masking effect of clouds is highly dependent on the intrinsic absorption strength of the specific molecular bands (Fauchez et al., 2022; Komacek et al., 2020; Pidhorodetska et al., 2020). Optically thick water and ice clouds systematically truncate the observable atmospheric path length (Lustig-Yaeger et al., 2023; Macdonald & Cowan, 2019). However, highly efficient absorbers in the mid-infrared, such as CO_2 and specific H_2O bands, exhibit significant resilience against this obscuration. The extreme absorption cross-sections of these molecules ensure that even minute gas concentrations remaining above the cloud deck keeping these features detectable (Fauchez et al., 2022; Pidhorodetska et al., 2020).
This complexity is further compounded by significant atmospheric modeling uncertainties. The TRAPPIST-1 Habitable Atmosphere Intercomparison (THAI) project was established to quantify discrepancies between different 3D General Circulation Models (GCMs). As outlined in the THAI protocol by Fauchez et al., 2020, differences in how models treat cloud microphysics and convection lead to varied predictions for identical planetary parameters. This is specifically demonstrated in THAI Part III (Sergeev et al., 2022), which reveals that models such as ROCKE-3D, ExoCAM, and LMD-G show major discrepancies in GCM treatments, particularly regarding cloud-top altitudes at the terminator, leading to significant uncertainties in detectability. Because high-altitude clouds raise the continuum level and shrink the observable absorption lines, Fauchez et al., 2022 found a maximum difference of over 40% between models in the predicted number of transits required to detect a modern Earth-like atmosphere. Models predicting higher cloud decks, such as ExoCAM, consequently require substantially more observing time than models predicting lower clouds.
A significant portion of current research, including the THAI project and studies like Pidhorodetska et al., 2020, focuses on the unique cloud distributions of tidally locked planets around M-dwarfs. These planets often exhibit persistent cloud decks near the substellar point that can extend to the terminator, significantly complicating observations. However, as noted by Doshi et al., 2022; Robinson, 2005, Earth is rarely used as a direct benchmark in these simulations, despite being the only terrestrial atmosphere where vertical cloud structures and their variability are understood with high precision.
Using the modern Earth as a reference model provides a ground truth for assessing the impact of clouds on spectral detectability. Unlike the permanent, thick cloud decks predicted for many tidally locked scenarios, the Earth's rapidly rotating atmosphere produces more complex, fragmented cloud patterns. This binary comparison—comparing a pristine, clear-sky Earth atmosphere to one with a complete, realistic cloud distribution—is essential for establishing observational limits (Komacek et al., 2020).

1.3. Research Question

How does the presence of clouds influence the detectability of molecular spectral features in exoplanet transmission spectra, and how do these effects vary with the star-planet radius ratio and orbital distance?

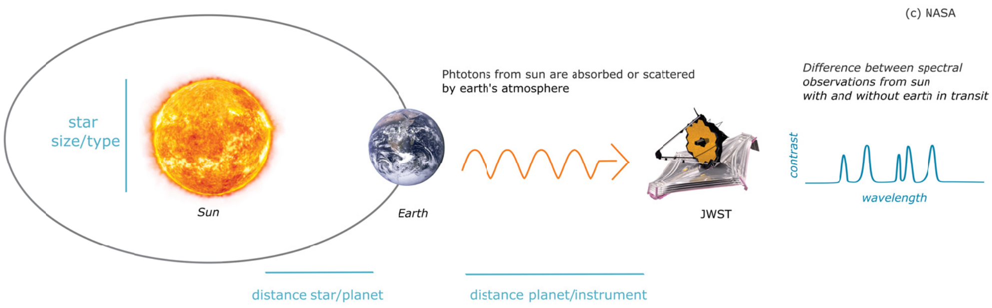

Figure 1. Schematic overview of a transit spectroscopy measurement: starlight passes through the planet's atmosphere and is filtered depending on its composition and structure. Key influencing parameters include the star's radius/type, the planet-star distance, and the viewing geometry from the instrument

To address this, the study compares two distinct scenarios: a clear-sky Earth analog and a cloudy atmosphere. Using the modern Earth as a reference model provides a ground truth for assessing the impact of clouds on spectral detectability. Unlike the permanent, thick cloud decks predicted for many tidally locked scenarios, the Earth's rapidly rotating atmosphere produces more complex, fragmented cloud patterns. This binary comparison—comparing a pristine, clear-sky Earth atmosphere to one with a complete, realistic cloud distribution—is essential for establishing observational limits (Komacek et al., 2020). Komacek et al., 2020 and Pidhorodetska et al., 2020 demonstrate that the presence of clouds can increase the number of required transits for robust detection by an order of magnitude. Therefore, evaluating the "cloudy vs. clear" contrast for an Earth analog provides a baseline for what telescopes like the JWST might realistically achieve when observing planets that may not exhibit the extreme cloud patterns of tidally locked worlds. This approach allows us to quantify how clouds alter the spectral shape and depth of signatures like CO_2, H_2O, and CH_4, which are primary targets for characterizing potential habitability.

Beyond cloud opacity, the observability of these signals is governed by two constraints. First, the star-to-planet radius ratio defines the baseline signal amplitude (Charbonneau et al., 1999). Second, the orbital distance creates a refractive floor that cuts off the lower atmosphere Betremieux and Kaltenegger, 2014.

The goal of this work is to establish a systematic baseline for these effects; a schematic overview of the setup is illustrated in Figure 1. By using the Planetary Spectrum Generator (PSG) to run a grid of simulations across different stellar types and distances, I aim to show how meteorological and physical limits compete. Ultimately, this clear-versus-cloudy comparison quantifies the signal suppression of molecular features in the presence of clouds.

2. Methods

2.1. Generating Transit Spectra

The Planetary Spectrum Generator (PSG) is a modular radiative transfer suite developed at NASA Goddard Space Flight Center, designed to synthesize spectra for a broad range of planetary bodies and observing geometries. For exoplanet studies, PSG is particularly effective at simulating transmission spectroscopy by integrating atmospheric structure, molecular spectroscopy, and instrument-specific noise models into a single computational framework (Villanueva et al., 2022).

At its core, PSG employs a line-by-line radiative transfer module. This approach calculates absorption cross-sections at extremely high spectral resolution by accessing the HITRAN database, which provides the transition parameters for hundreds of molecular species (Gordon et al., 2022). For transit simulations, the generator computes the slant optical depth through the planetary limb, accounting for the exponential increase in path length as light grazes the lower, denser layers of the atmosphere.

A critical feature of this study is PSG's treatment of scattering and extinction. Rayleigh scattering is calculated based on the background gas composition, while clouds and aerosols are modeled using Mie theory. This allows for the inclusion of specific cloud deck properties, such as particle size distribution and optical depth, which are essential for simulating the gray opacity that masks molecular features.

For this study, PSG's "Atmospheric" and "Instrument" modules are utilized to generate synthetic JWST-like observations. The spectra are typically output as C(λ) in parts per million (ppm). By utilizing the 3D-profile interface, the vertical placement of cloud layers can be precisely controlled, enabling a direct comparison between pristine, clear-sky atmospheres and a simulation of Earth's atmosphere with clouds. This framework provides the sensitivity to quantify how much of the signal is lost to cloud masking under varying stellar and geometric conditions.

In this study, PSG was employed to simulate synthetic transmission spectra of Earth observed with theoretical JWST observations. As detailed by Gardner et al., 2006, the combined capabilities of JWST's Near-Infrared Spectrograph (NIRSpec, covering 0.6–5.0 μm) and the Mid-Infrared Instrument (MIRI, covering 5.0–29 μm) span the crucial observation window. Access to this continuous near- to mid-infrared domain allows observers to evaluate the near-infrared H_2O bands and the mid-infrared signatures within a single unified framework. The simulations aim to assess the influence of cloud altitude and star-planet geometry on the detectability of key molecular features, particularly CO_2, H_2O, and CH_4. To effectively capture these absorption bands, a wavelength range of 1 to 10 μm was selected for the analysis.

The simulations for the 3D input data are provided by the ICOsahedral Non-hydrostatic Atmospheric model ICON A (Giorgetta et al., 2018), which was tuned based on the Atmospheric Model Intercomparison Project (AMIP). As originally established by Gates, 1992, the AMIP experiment provides a standardized protocol to evaluate and intercompare atmospheric models under realistic conditions. It aims to simulate the climate of recent decades by utilizing prescribed, time-varying boundary conditions, specifically observed sea surface temperatures and sea ice distributions (Gates, 1992). The utilized climate simulation is in equilibrium and accurately reflects present-day atmospheric conditions. Structurally, the model comprises 47 vertical layers and incorporates both ice and liquid water clouds. Although the dataset spans

the entire month of May 1983 at a daily resolution, the subsequent analysis focuses on the initial timestep (May 1st) as a representative atmospheric snapshot. To generate realistic atmospheric states, the 3D climate model output of the ICON general circulation model (GCM) was used as the primary input. The ICON data set provides spatially resolved fields for temperature, pressure, water vapor, ice cloud content and liquid water cloud content. These variables were formatted into PSG-compatible files and processed using the PSG "Globe" application.
For each simulation, a PSG configuration file was created, defining the planetary, stellar, atmospheric, and instrumental parameters; examples from climate models other than ICON were used as a broad framework (NASA, 2025). The key settings are summarized in the Appendix 2, where the varied parameters are highlighted in bold. In particular, the simulations span different spectral types (M8 to G0), star-planet distances (0.01 to 1.00 AU), and clear-sky and cloudy conditions.
Figure 2 visualizes the workflow.

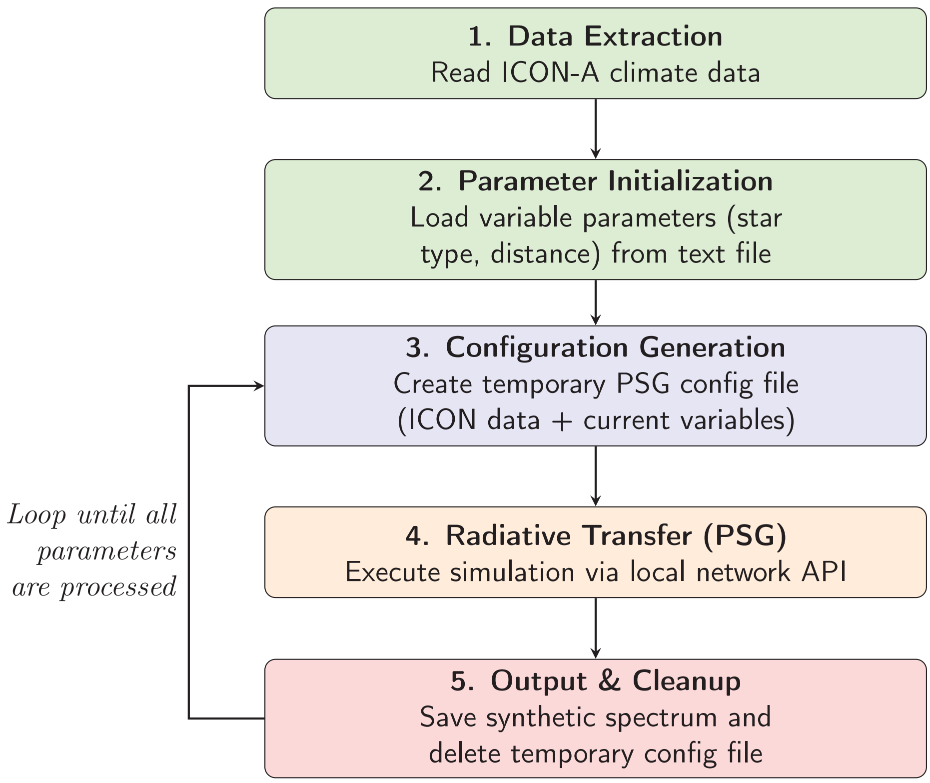

Figure 2. Workflow of the Python-based framework used to systematically generate synthetic transmission spectra. The process iterates over a predefined grid of stellar types and orbital distances and cloudy and clear-sky conditions.

The main experiment contrasts two distinct atmospheric scenarios: a fully clouded atmosphere based on the original ICON distribution and a completely cloud-free atmosphere. Rather than examining every roach, this allows for a direct comparison of cloud effects on transmission depth and spectral feature detectability. Rather than examining every roach, this allows for a direct comparison of cloud effects on transmission depth and spectral feature detectability. The PSG geometry was set to 'Observatory' mode, with a space-based viewing altitude of 1 parsec and a full planetary disk fraction. The instrument model assumed an idealized JWST

setup without noise. To simulate transmission spectra under realistic atmospheric conditions, the 3D climate model data from the ICON simulations were integrated with the PSG. While the Python-based framework designed to automate this workflow was developed by the author, the computational execution of the PSG simulations was carried out by the supervisor, Aiko Voigt. The simulation process systematically evaluated the entire parameter grid. For each run, the stellar properties—specifically spectral type, effective temperature, radius, and star-planet distance—were updated to reflect the configurations shown in Table 1, as well as one scenario of the whole grid with a clear-sky atmosphere and one scenario considering the clouds from the ICON simulation.
The selection of stellar types and orbital distances for this parameter grid was designed to bridge the gap between two fundamental benchmark scenarios. The lower boundary of the grid is anchored by the TRAPPIST-1 system, which represents a highly favorable target for near-term JWST observations—an Earth-sized planet in a tight orbit around an ultra-cool M8 dwarf (Gillon et al., 2017). The upper boundary is defined by the modern Earth-Sun analog, a G2-type star at an orbital distance of 1.0 AU, augmented by a slightly larger G0 star to provide a wider observational range. The intermediate spectral types (M5, M3, K5, and K0) and orbital distances (ranging from 0.05 to 0.8 AU) were selected to systematically fill this parameter space, creating a comprehensive matrix. To ensure physical consistency across this grid, the corresponding stellar parameters were adopted from standard main-sequence relations based on Christiansen et al., 2025.
It is important to emphasize that this parameter grid is a theoretical construct intended to isolate and quantify the effects of varying star-to-planet radius ratios and orbital distances. Consequently, many of these generated combinations do not represent physically realistic or habitable environments. For instance, an Earth-analog orbiting a G0 star at 0.01 AU would be completely desiccated, while a planet at 1.0 AU around an M8 dwarf would be entirely frozen, both falling far outside the classical habitable zone limits established by Kopparapu et al., 2013. By treating these parameters as an independent mathematical grid, this approach allows for a systematic evaluation of how cloud opacity and atmospheric refraction attenuate spectral features across all conceivable observational geometries, regardless of their immediate astrobiological viability.
This study adopts the perspective of 'Earth as an Exoplanet' by using two primary examples as a frame of reference: our own Earth-Sun system (a G2 star) and an approximation of the TRAPPIST-1e system (an M8 star). Comparing these two cases illustrates the fundamental 'astronomical barrier' of solar-type hosts while highlighting why ultra-cool dwarfs like TRAPPIST-1 represent the most promising targets for atmospheric characterization. To systematically investigate the transition between these two extremes, the simulations included a grid of stellar types with varying radii, temperatures, and planet-star distances. The complete grid is shown in Table 1. Each row represents a distinct spectral type, while the corresponding distances span a range of potential orbital separations. This allows for a comparative analysis of the star-to-planet ratio and its impact on transit depth and spectral contrast, and therefore, the impact of clouds on these parameters.

2.2. Post-processing and analysis

Once the synthetic transmission spectra were generated using PSG, the data had to be processed to quantify how well specific molecular features could actually be detected. To gain a first

Spectral Type	Radius ($R_\odot$)	Temperature (K)	Distances (AU)
M8	0.1	3000	0.01 0.05 0.10 0.20 0.50 0.80 1.00
M5	0.2	3500	0.01 0.05 0.10 0.20 0.50 0.80 1.00
M3	0.3	4000	0.01 0.05 0.10 0.20 0.50 0.80 1.00
K5	0.5	4800	0.01 0.05 0.10 0.20 0.50 0.80 1.00
K0	0.8	5200	0.01 0.05 0.10 0.20 0.50 0.80 1.00
G2	1.0	5778	0.01 0.05 0.10 0.20 0.50 0.80 1.00
G0	1.2	6000	0.01 0.05 0.10 0.20 0.50 0.80 1.00

Table 1. Stellar parameter grid used in PSG simulations, varying spectral type, stellar radius, effective temperature, and planet-star distance.

intuitive understanding of how clouds attenuate the planetary signal, a Spectral Difference Analysis was performed. For each scenario, a difference spectrum $\Delta C(\lambda)$ was generated by subtracting the clear-sky contrast (C_{clear}) from the cloudy reference (C_{cloudy}):

$$\Delta C(\lambda) = C_{\text{cloudy}}(\lambda) - C_{\text{clear}}(\lambda) \tag{2.1}$$

This approach effectively nulls the baseline of the transit and isolates the specific portions of the signal that are masked by cloud opacity.
The goal was to find a way to compare the spectra across various scenarios—different star types, distances, and cloud conditions—without getting lost in the complexity of the full spectral output. Instead of looking at every single data point, the focus is on a few key molecular species that serve as primary indicators of habitability and atmospheric chemistry. As illustrated in Figure 3, specific wavelength windows for H_2O, CH_4, and CO_2 were defined and serve as representatives of the impact of cloud masking. The following standardized intervals were chosen to ensure that even pressure-broadened line wings are fully captured, aligning with the sensitivities of JWST instruments like NIRSpec and NIRCam:

- **Water ($\mathbf{H_2O}$):** Two distinct intervals were selected to capture the full range of water vapor activity. The first window (1.30 - 1.60 μm) covers the classic near-infrared band, which is highly susceptible to Mie scattering by cloud particles. The second window was set in the mid-infrared (5.50 – 7.50 μm), where H_2O exhibits its strongest rotational-vibrational absorption. This dual-band approach allows for the study of how clouds affect water signatures differently depending on the intrinsic absorption strength of the specific band, as strong mid-infrared absorbers are known to be more robust against cloud masking (Fauchez et al., 2022; Pidhorodetska et al., 2020).

- **Methane ($\mathbf{CH_4}$):** 3.10 - 3.70 μm. This range covers the strong ν_3 fundamental band (Betremieux & Kaltenegger, 2014).

- **Carbon Dioxide ($\mathbf{CO_2}$):** 4.00 - 4.70 μm. It is one of the most intense features in the entire spectrum, often remaining detectable even when lower-altitude clouds are present. (Fauchez et al., 2022)

To further analyze how the ICON-simulated cloud cover affects the detectability of atmospheric gasses, two main metrics were defined: the Global Spectral Loss and the Feature-Specific Loss. The comparison is conducted between a cloud-free reference scenario (C_{clear}) and the scenario including ICON cloud physics (C_{cloudy}). The Global Spectral Loss (L_{global}) serves as

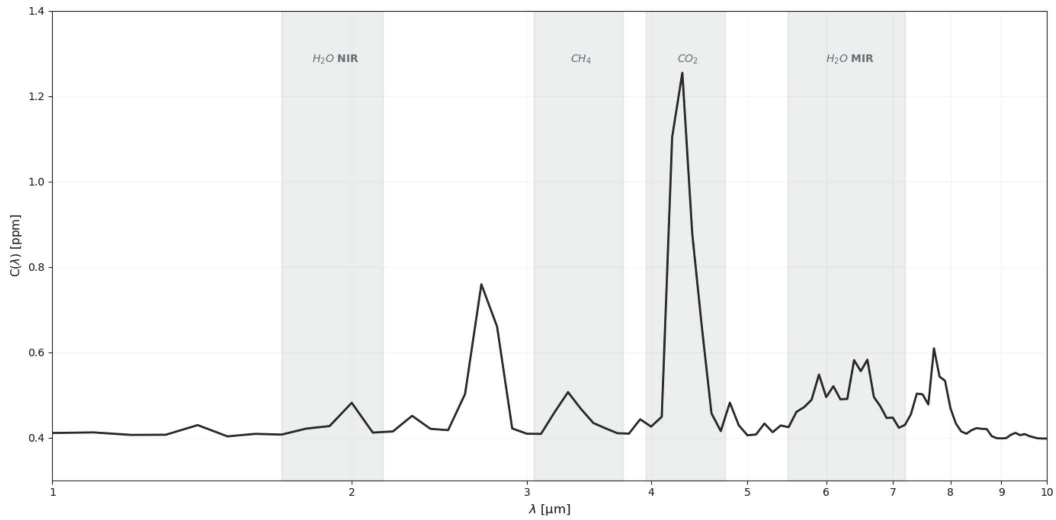

Figure 3. Synthetic transmission spectrum (Transit Depth in ppm vs. Wavelength in μm) for an Earth-like atmosphere orbiting a G2-type star at a distance of 1.0 AU. The spectrum is calculated for a clear-sky scenario. The shaded areas indicate the wavelength intervals defined to quantify the detectability key habitability indicators (H_2O, CH_4, CO_2). Two H_2O intervals were used to compare near-infrared (NIR) and mid-infrared (MIR) absorption characteristics.

a measure of the overall "muting" of the spectrum. It is calculated by first determining the ratio $R(\lambda) = C_{cloudy}(\lambda)/C_{clear}(\lambda)$ for every wavelength point. The global loss in percent is then derived from the average of these ratios across all N wavelength points:

$$L_{global}[\%] = \left(\frac{1}{N} \sum_{i=1}^{N} R(\lambda_i) - 1 \right) \times 100 \tag{2.2}$$

The reduction in spectral amplitude caused by clouds is hereafter referred to as the muting effect. This is quantified by the Feature Specific Loss (L_{feat}), which measures how much molecular information is lost due to the gray opacity of the cloud layers. This metric measures the reduction in the amplitude of characteristic absorption bands. The amplitude (A) is defined as the difference between the local maximum (peak) and the local minimum (baseline) within a specific wavelength interval:

$$A = \max(C_{\lambda_{start} \ldots \lambda_{end}}) - \min(C_{\lambda_{start} \ldots \lambda_{end}}) \tag{2.3}$$

The resulting loss for a specific gas is:

$$L_{feat}[\%] = \left(1 - \frac{A_{cloudy}}{A_{clear}} \right) \times 100 \tag{2.4}$$

A feature loss of 0% indicates no muting effect by clouds, whereas a value of 100% represents complete masking by the ICON cloud layers, rendering the gas undetectable even for completely ideal JWST observations.

2.3. Use of Artificial Intelligence (AI) Tools

During the preparation of this thesis, AI tools were employed as supportive aids to facilitate various stages of the research and writing process. In the initial phases, **ChatGPT** (OpenAI) was utilized as a collaborative tool to discuss relevant scientific literature, gain a deeper understanding of the PSG and its configuration, and assist in developing the structure of the methodology. During the drafting phase, **Google Gemini** was employed to refine the academic English, improve the stylistic flow of the text, and provide technical assistance with the esthetic enhancement of data visualizations. All AI applications were used strictly in an advisory and supportive capacity. Their usage adhered to the guidelines for good scientific practice and did not replace any independent scientific contributions. The generated outputs were critically evaluated, questioned, adapted, and contextualized by the author. The selection and interpretation of sources, the development of the scientific argumentation, the quantitative analysis of the data, and the final formulation of the text remain entirely the author's own independent work. The author bears sole responsibility for the content, accuracy, translations, and conclusions presented in this thesis.

3. Results

Before examining the complex meteorological influence of clouds, it is imperative first to establish the fundamental geometric barrier of the simulated observations. Therefore, it is necessary to first quantify the maximum observable pressure (p_{max}) as described in Equation 1.6, due to atmospheric refraction. Evaluating this refractive floor across the parameter grid reveals in which specific planet-star configurations it is physically possible to probe the lower atmosphere, setting an absolute baseline for detectability.
Figure 4 illustrates the maximum observable pressure p_{max} due to atmospheric refraction as a function of stellar radius and orbital distance, assuming the size of Earth. Each point in the parameter space represents the pressure level below which stellar light is bent away and no longer contributes to the transmission spectrum. The black contour marks Earth's surface pressure (1013 hPa). Systems lying below this line permit transmission down to the surface, while those above are optically cut off at higher altitudes. For example, Earth in the Sun–Earth configuration (blue circle) exhibits a cutoff at approximately 247 hPa, meaning that transmission spectra can only probe the upper troposphere. In comparison, TRAPPIST-1e (blue cross), orbiting a much smaller star at a lower distance, allows transmission to the surface (1067 hPa). This shows why compact M-dwarf systems offer improved access to lower atmospheric layers for observations.

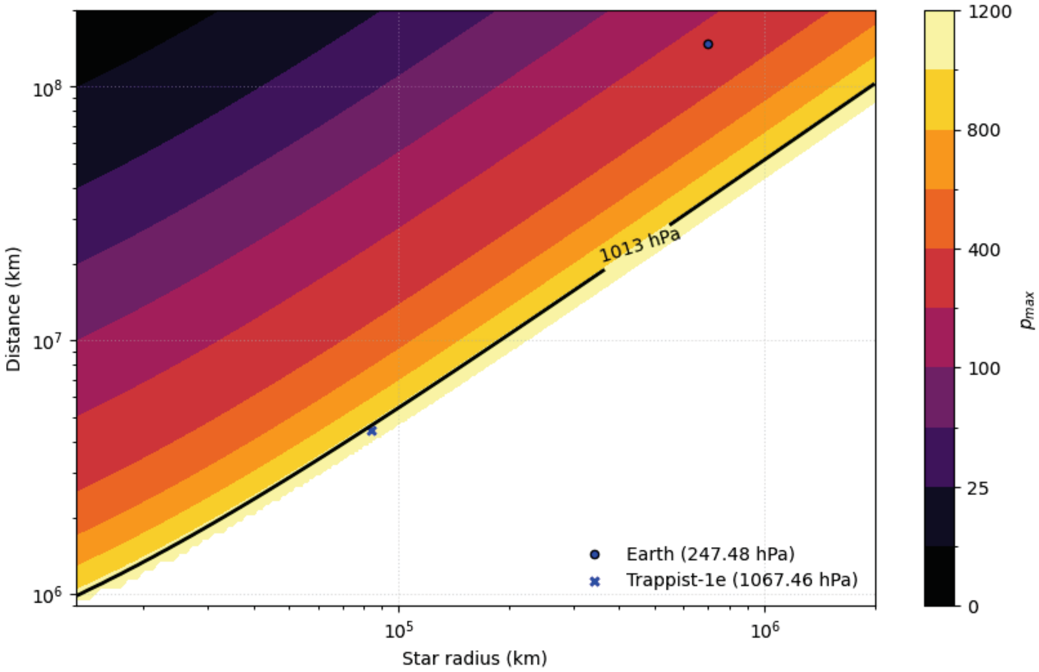

Figure 4. Maximum observable pressure p_{max} level due to refraction as a function of stellar radius and star–planet distance. The black contour indicates the surface pressure of Earth (1013 hPa); values below this line allow transmission down to the surface. Earth and TRAPPIST-1e are shown for reference, with their respective p_{max} values in parentheses.

Having established the geometric limits of atmospheric refraction, it is now clear how deep transmission spectroscopy can theoretically probe into the atmospheres across the simulated parameter grid. However, to fully grasp the implications for actual observations and to understand the specific muting effect of clouds, it is necessary to examine how water is vertically distributed within these accessible layers. Figure 5 illustrates the vertical profiles of relative humidity, ice water content, and liquid water content of the ICON simulation and, therefore, the input data for PSG. The horizontal black line marks the refractive limit for an Earth-Sun analog, which is approximately located at an altitude of 12.6 km, corresponding to a pressure of approximately 0.24 bar. Light rays passing below this critical altitude are deflected too strongly to reach a distant observer.

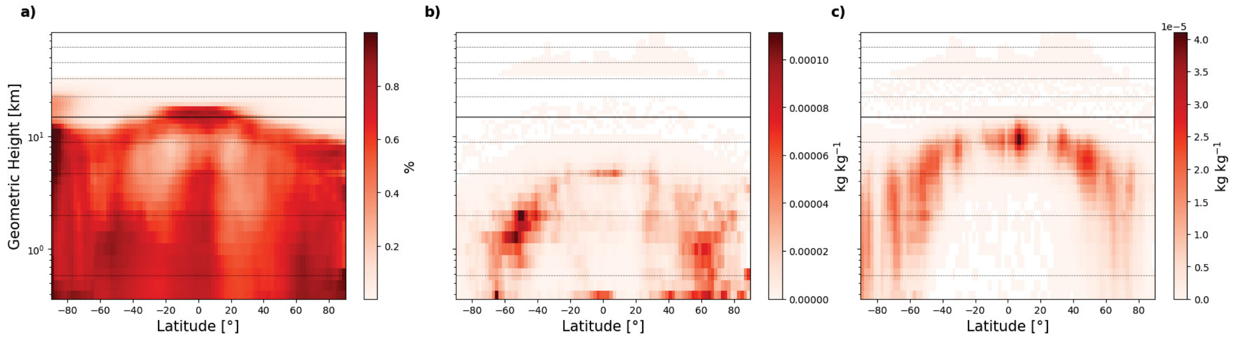

Figure 5. Vertical atmospheric profiles from the ICON-A climate simulation. The panels display the zonal mean distributions of (a) relative humidity, (b) ice water content, and (c) liquid water content as a function of latitude and geometric height. The solid horizontal black line indicates p_{max} for an Earth-Sun scenario, located at an altitude of approximately 12 km.

Building on these geometric considerations, Figure 6 shows how these theoretical differences in transit depth manifest in synthetic spectra. By comparing a solar-type G2 host (an Earth-Sun analog) in panel (a) with an M8 dwarf (resembling the TRAPPIST-1 system) in panel (b), the practical impact of the star-to-planet ratio becomes immediately apparent. The most obvious difference is the magnitude of the transmission signal. This is a direct consequence of the star-to-planet radius ratio discussed in 1.2.1. The much smaller radius of the M8 dwarf leads to signals about a 100 times stronger. In the M8 case, the transit depths range from about 10 to 150 ppm, offering a favorable signal-to-noise ratio for atmospheric characterization. In comparison, the signals for the G2 scenario remain consistently below 1.5 ppm. This truly highlights why detecting terrestrial atmospheres around Sun-like stars is such a massive challenge; with instruments like the JWST, these signals are often pushed right to the edge of what is measurable when noise is considered, making JWST and transmission spectroscopy ineffective for these cases.
The influence of the orbital distance also plays out quite differently in these two cases. In the M8 scenario, the spectral signatures remain easy to distinguish across all the simulated distances. However, in the G2 case, a peculiar "pile-up" occurs. For orbits within roughly 0.2 AU, the spectra start to overlap and effectively saturate at a certain contrast level. This is where the physical limit of refraction becomes clearly visible.

To further investigate these trends across a broader range of stellar hosts, Figure 7 presents a comprehensive grid of transmission spectra from G0 to M8. This comparison includes both clear-sky (solid lines) and cloudy atmospheres (dashed lines) to illustrate the combined influence of stellar type, orbital distance, and cloud coverage. As shown in the panels, the magnitude of the transit depth continues to scale with the stellar radius, as previously established. A key observation in panels (a) through (f) is the "pile-up" effect of the spectra for planets at closer orbital distances. For hosts warmer than an M8 dwarf, the spectra for orbits within approximately 0.2 AU tend to converge, regardless of whether clouds are present or not. It is only in panel (g), representing the M8 host, that a clear separation between all simulated distances remains visible across the entire range. The impact of cloud coverage, visualized by the dashed lines, reveals a muting effect on the absorption features. While the characteristic molecular bands of water and methane are still present, their amplitudes are reduced compared to the clear-sky scenarios. Interestingly, for planets at larger orbital distances (e.g., the outermost simulated

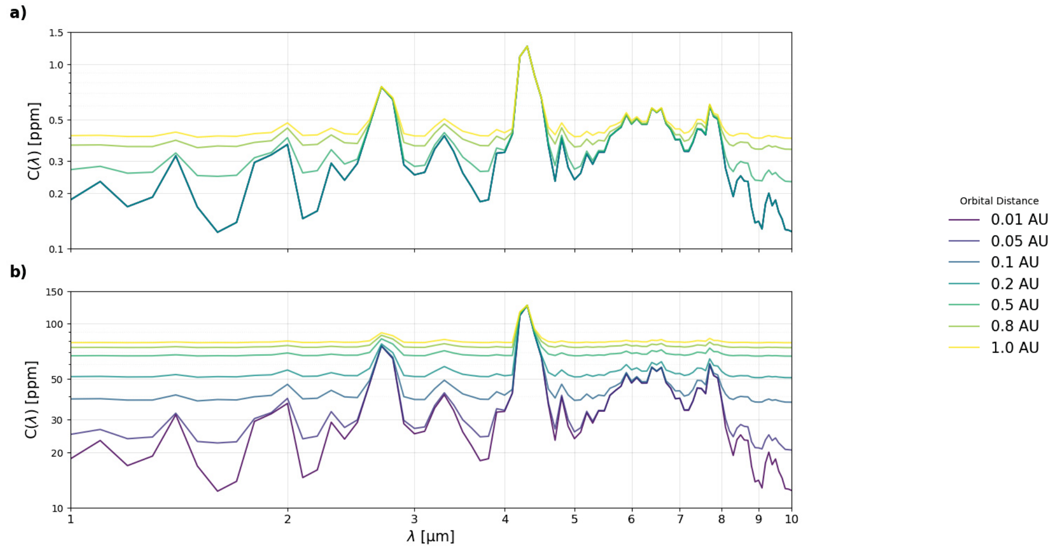

Figure 6. Synthetic transmission spectra from ICON simulations across two distinct stellar environments: (a) a solar-type G2 star and (b) an ultra-cool M8 dwarf. All spectra represent clear-sky conditions. Each curve corresponds to a specific orbital distance.

orbits), the difference between the clear and cloudy cases becomes increasingly marginal, with the spectra nearly overlapping in some instances. Once p_{max} rises above the physical altitude of the primary cloud decks, the lower atmosphere becomes completely obscured by refraction. At this point, the transmitted light only probes atmospheric layers that are physically cloud-free, rendering the presence or absence of deep clouds irrelevant to the observed spectrum.

While the previous grid focused on the evolution of spectra for individual stars, Figure 8 fixes the orbital distance in each panel to highlight the impact of the host star type. This perspective directly visualizes what was defined in the introduction as the "Astronomical Barrier" (1.2.1) of transmission spectroscopy: the fundamental dependency of the signal on the planet-to-star radius ratio.
As each panel shows, the transit depth is not uniform across the stellar sequence. Even though the simulated planet remains an Earth-analog in every case, the transit depth increases significantly as the host star becomes smaller and cooler. Moving from the solar-type G0 host (bottom of the panels) to the M8 dwarf (top of the panels), the signal amplitude rises by nearly two orders of magnitude. Because the y-axis is kept consistent across these panels, the vertical "spread" of the curves serves as a direct measure of this geometric advantage. It is important to note that Figure 8 utilizes a logarithmic y-axis to accommodate the vast range of contrasts across the stellar sequence. While the peaks for G-type stars may visually appear equally or even more pronounced relative to their baseline, this is purely a mathematical artifact of the logarithmic scale. In absolute terms (ppm), the signal amplitude added by the atmospheric absorption is minute for G-stars compared to the M-dwarf scenarios. The absolute feature amplitudes, which ultimately dictate the observational detectability, are explicitly quantified on a linear scale later on in Figure 11, confirming the geometric advantage of M-dwarf hosts.
A further key observation is the varying impact of cloud coverage. The difference between the clear-sky (solid) and cloudy (dashed) spectra—the muting effect—is not constant. It becomes

most pronounced for the smallest host stars and the closest orbital distances (panels a–c). Around M-dwarfs, the spectral features are more pronounced. Crucially, the refractive floor in these compact systems lies deep enough to fully expose the primary cloud decks, which in turn allows the clouds to mask a much larger absolute portion of the signal.

To quantify the impact of cloud opacity on the transit signal, Figure 9 presents the spectral differences calculated according to Equation 2.1. The magnitude of this effect exhibits a strong dependence on the stellar type. For the solar-type G0 star (panel a), the absolute difference remains negligible, consistently staying below 0.1 ppm across all wavelengths. However, for smaller host stars, this masking effect becomes significantly more pronounced. In the case of the M8 dwarf (panel g), clouds reduce the transit signal by up to 15 ppm at close orbital distances.
Furthermore, the spectral response to varying orbital distances reveals distinct patterns. For G- and K-type hosts (panels a–d), the spectra at close orbital separations (within 0.2 AU) are nearly degenerate and overlap. The divergence of these curves becomes apparent primarily for cool M-dwarfs, where the signals separate clearly across all simulated distances
To ensure conciseness and avoid repetitive visualizations, only the difference spectra partitioned by stellar type are presented in this section. However, the corresponding plots partitioned by orbital distance, which further illustrate the consistency of these scaling effects, are provided in the Appendix A for further reference.

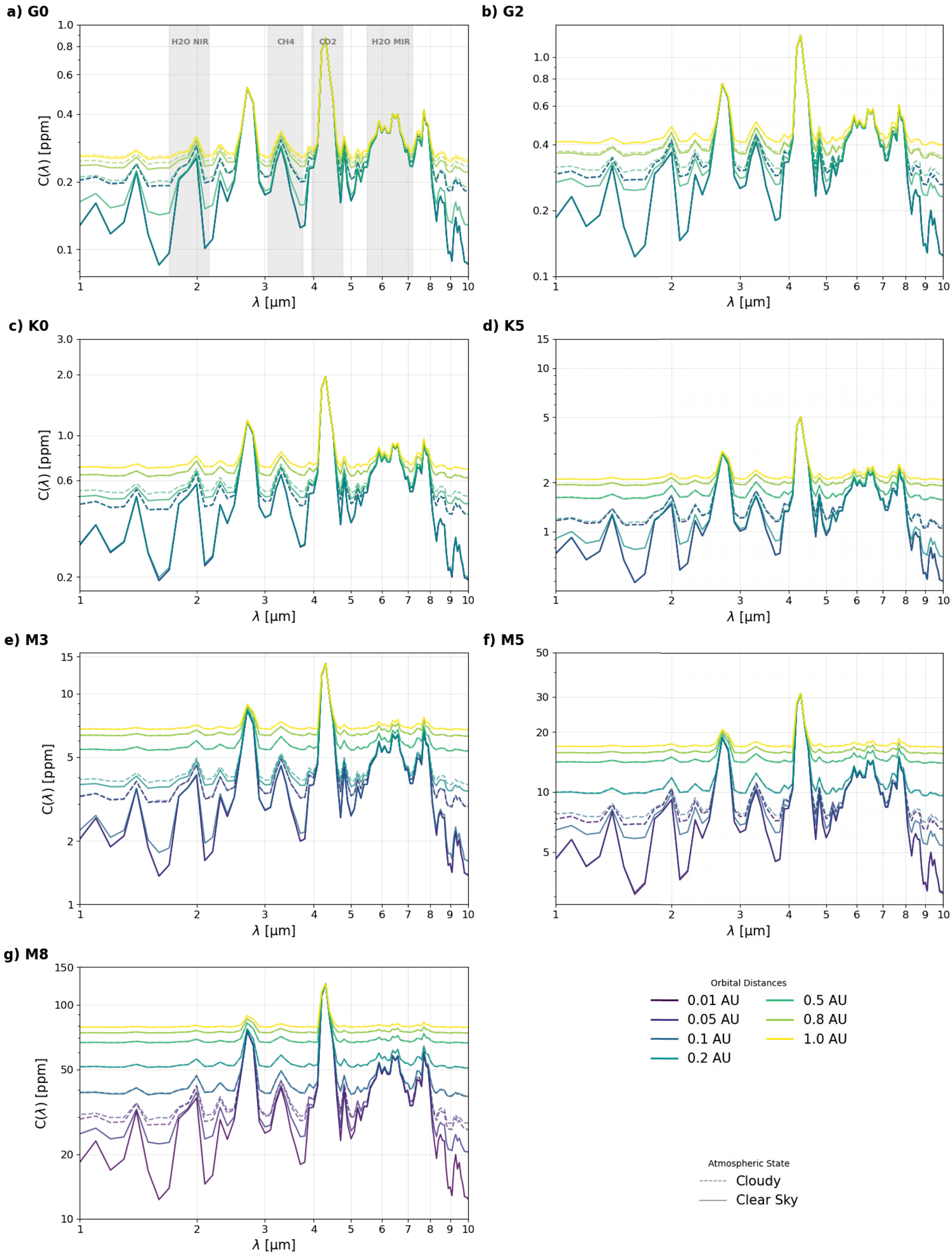

Figure 7. Influence of Refraction and Cloud Coverage across Different Stellar Environments. The panels display synthetic transmission spectra for various host stars: a) G0, b) G2, c) K0, d) K5, e) M3, and f) M5, g) M8. Solid lines indicate clear-sky conditions, while dashed lines show the cloudy case. The comparison illustrates the physical limit of refraction, appearing as a "pile-up" and saturation of the signal at close orbital distances (most prominent in panels a–c). Furthermore, the dashed lines visualize the muting effect of clouds on the spectral features. Note that the y-axis scales vary significantly between panels to accommodate the different signal magnitudes across the stellar sequence.

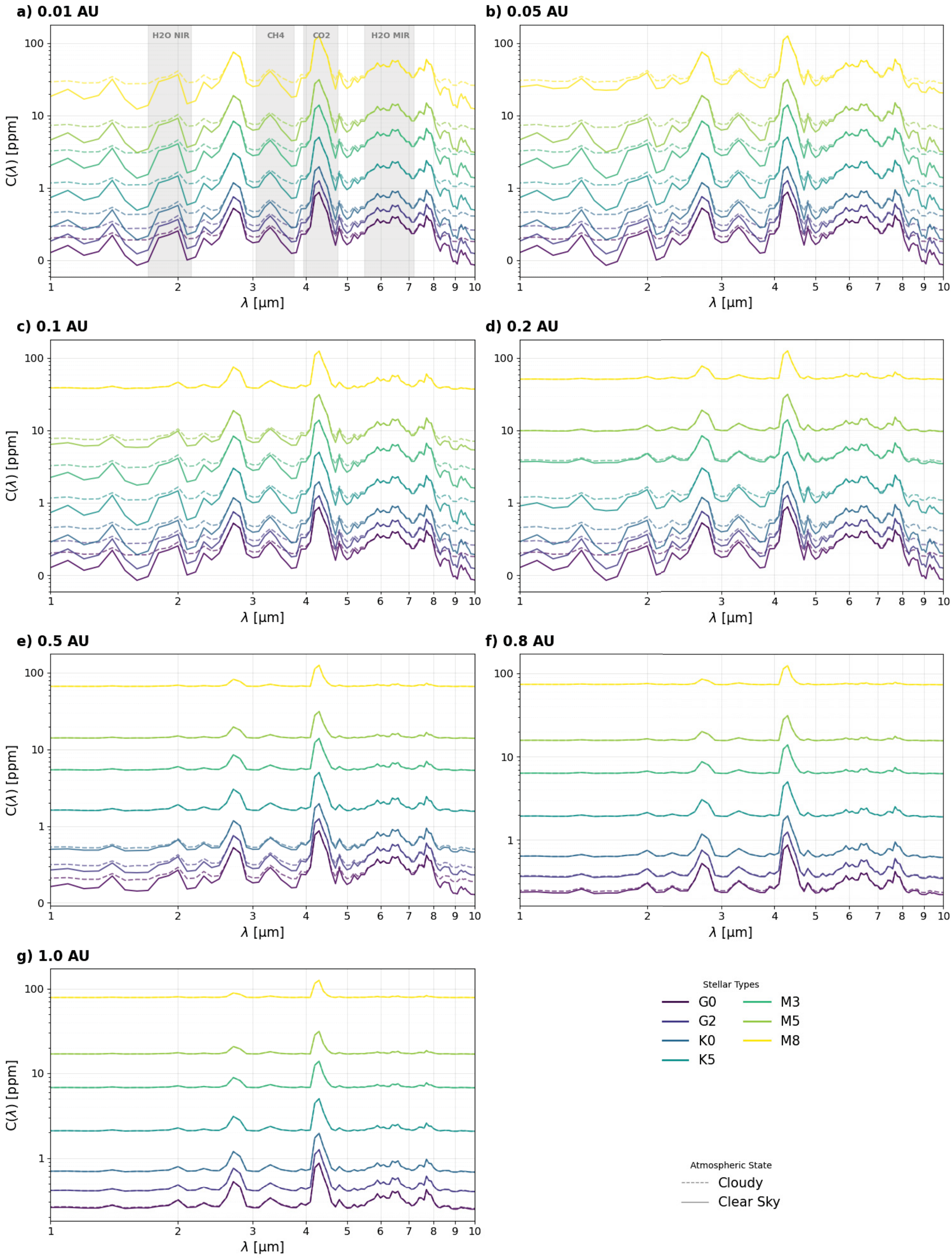

Figure 8. The panels illustrate the impact of the stellar host type for specific orbital configurations: a) 0.01 AU, b) 0.05 AU, c) 0.1 AU, d) 0.2 AU, e) 0.5 AU, and f) 0.8 AU, g) 1.0 AU. Solid lines represent clear-sky conditions, while dashed lines show the cloudy case. In contrast to previous figures, the y-axis scaling is kept consistent across the panels to emphasize that the separation of the spectra is a direct result of the varying planet-to-star radius ratio. The results show that the distinction between clear and cloudy atmospheres is most pronounced for planets in close proximity to their host stars (a–c)

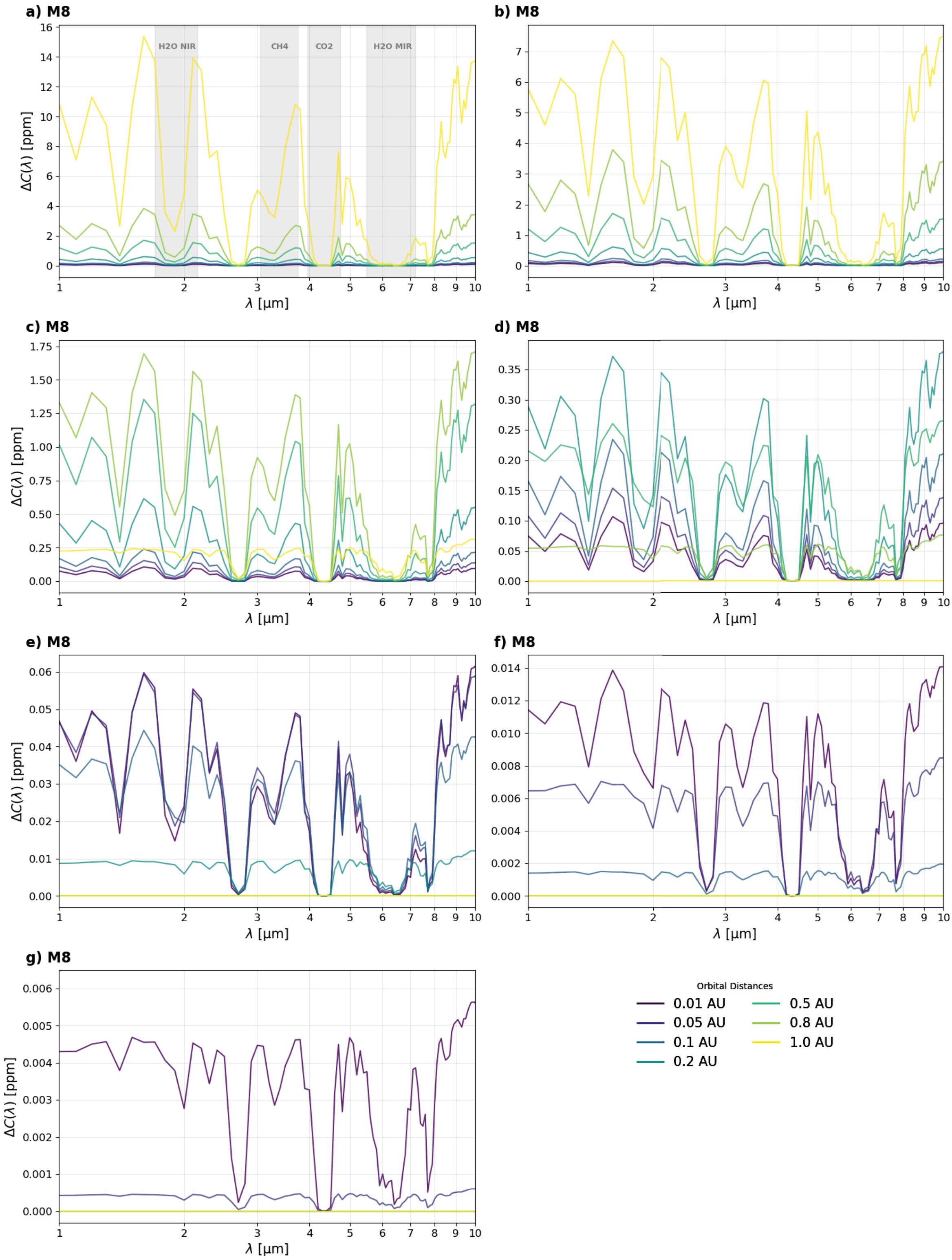

Figure 9. Spectral Difference ($\Delta C(\lambda)$) across the stellar grid. Each panel displays the absolutely "lost" transit signal, calculated as the difference between the clear-sky and cloudy scenarios ($C_{cloudy} - C_{clear}$). Results are shown for host stars from (a) G0 to (g) M8. Note that the y-axis scales are adapted for each panel to emphasize the individual spectral features.

To quantify the overall impact of the cloud deck on the transit signal, L_{global} was calculated according to equation 2.2. This metric represents the relative increase in the spectral contrast caused by the additional cloud opacity. Figure 10 illustrates the magnitude of this continuum shift across the stellar grid as a function of orbital distance. At extremely close orbital separations (0.01 AU), the effect is maximized, altering the contrast by over 20% for almost all stellar types. However, as the orbital distance increases, this relative difference diminishes due to the rising refractive floor. The distance at which this geometric decoupling occurs depends strictly on the stellar type: For the M8 dwarf, the continuum shift caused by clouds becomes negligible at orbital distances beyond 0.1 AU. In contrast, for the G0 star, a measurable inflation of the contrast persists, declining continuously from 0.2 AU but never reaching zero, even at 1.0 AU.

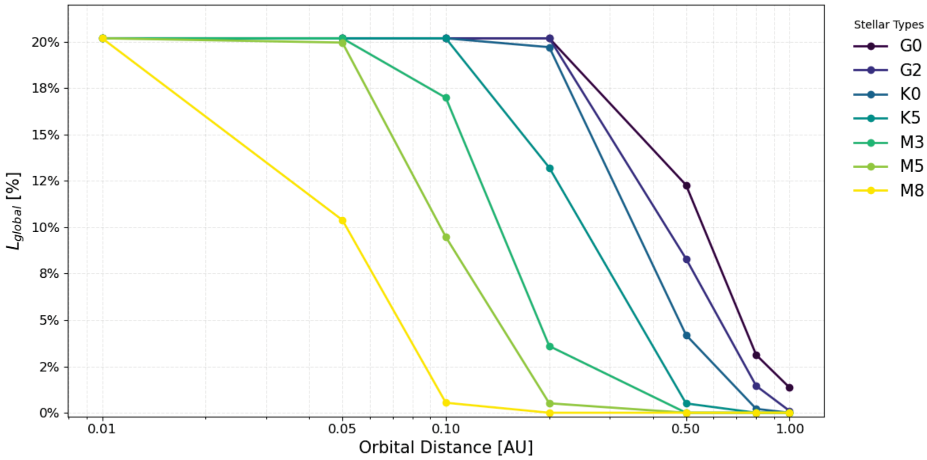

Figure 10. Global spectral loss in percent caused by cloud coverage. The plot shows how much of the total transit signal is lost because the clouds prevent the instrument from probing the deeper layers of the atmosphere. The loss is shown for different stellar types across a range of orbital distances.

Before assessing relative signal degradation, first examining the absolute feature amplitudes (A) of the key molecular bands is necessary. While the global loss reflects the overall shift in the continuum caused by clouds, the feature amplitude (Equation 2.3) quantifies the physical strength of individual absorption peaks. Figure 11 presents A for the four targeted spectral windows: (a) H_2O NIR, (b) H_2O MIR, (c) CH_4, and (d) CO_2.

As expected from the refractive limits discussed earlier, amplitudes generally decline with increasing orbital distance across all stellar types. However, this attenuation is highly species-dependent. The CO_2 band exhibits remarkable stability, showing almost no dependence on orbital separation and maintaining a strong, easily detectable signal of nearly 100 ppm for the M8 dwarf. Conversely, the near-infrared H_2O band (panel a) is extremely sensitive to the orbital distance, experiencing a steep drop in amplitude for wider orbits. The CH_4 band (panel c) likewise provides a high absolute contrast; particularly around M8 dwarfs, where its signal surpasses that of a G0 host by nearly two orders of magnitude.

Overall, these raw signal strengths underscore the profound observational advantage of late-type stars. The significantly higher baseline signals of M8 dwarfs facilitate atmospheric characterization even when clouds are present. Furthermore, comparing these absolute amplitudes directly quantifies the fundamental masking effect of clouds: clear-sky amplitudes consistently exceed their cloudy counterparts across all configurations. This amplitude gap, which represents the absolute suppression of the planetary signal, is most severe in the H_2O NIR band.

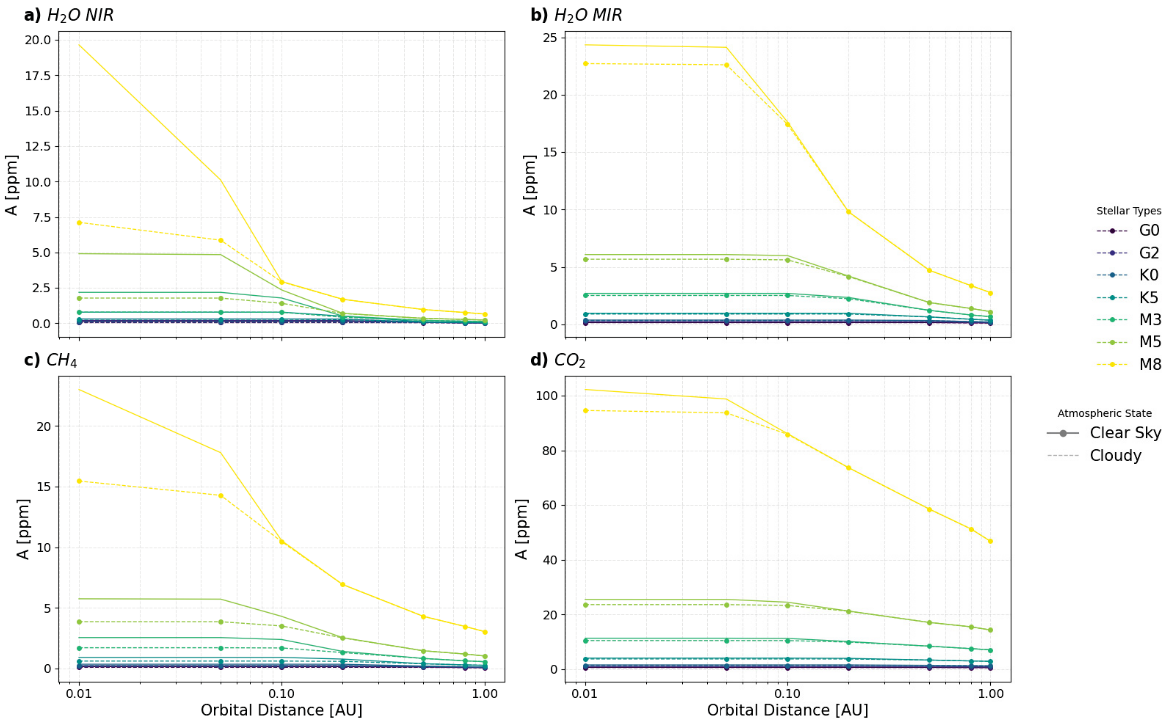

Figure 11. Absolute feature amplitudes (A) in ppm for the four investigated spectral windows: (a) H_2O NIR, (b) H_2O MIR, (c) CH_4, and (d) CO_2 . The plots show the physical signal strength across different stellar types and orbital distances in the cloudy scenario. While the H_2O signals—particularly in the near-infrared (a)—show a strong dependence on orbital distance, the CO_2 features (d) remain remarkably stable. This illustrates that CO_2 is largely unaffected by cloud decks, maintaining a high and consistent signal regardless of the orbital separation.

A detailed examination of L_{feat} in Figure 12 reveals a significant variance in the masking effect caused by clouds across the four selected windows. A substantial signal degradation of up to 65% is primarily observed in the near-infrared H_2O band (panel a) and up to 35% in the CH_4 band (panel c). Conversely, the mid-infrared H_2O band (panel b) and the CO_2 band (panel d) prove to be robust, with the signal loss remaining consistently below 10% across the entire parameter space.

A crucial finding is the distinct dependence of this masking effect on stellar type and orbital distance. For the Sun-like G0 star, the molecular signatures never fully recover the amplitude of a clear-sky spectrum ($L_{feat} > 0$ across all distances), even at the maximum simulated distance of 1.0 AU. In these systems, a permanent residual influence of the cloud coverage remains measurable. In contrast, the M8 dwarf demonstrates a much more rapid recovery from cloud-induced signal loss. At an orbital distance of approximately 0.1 AU, the feature loss for most gasses drops to near zero. This indicates that for small, cool stars at wider orbits, the observable atmospheric layers are situated entirely above the primary cloud decks.

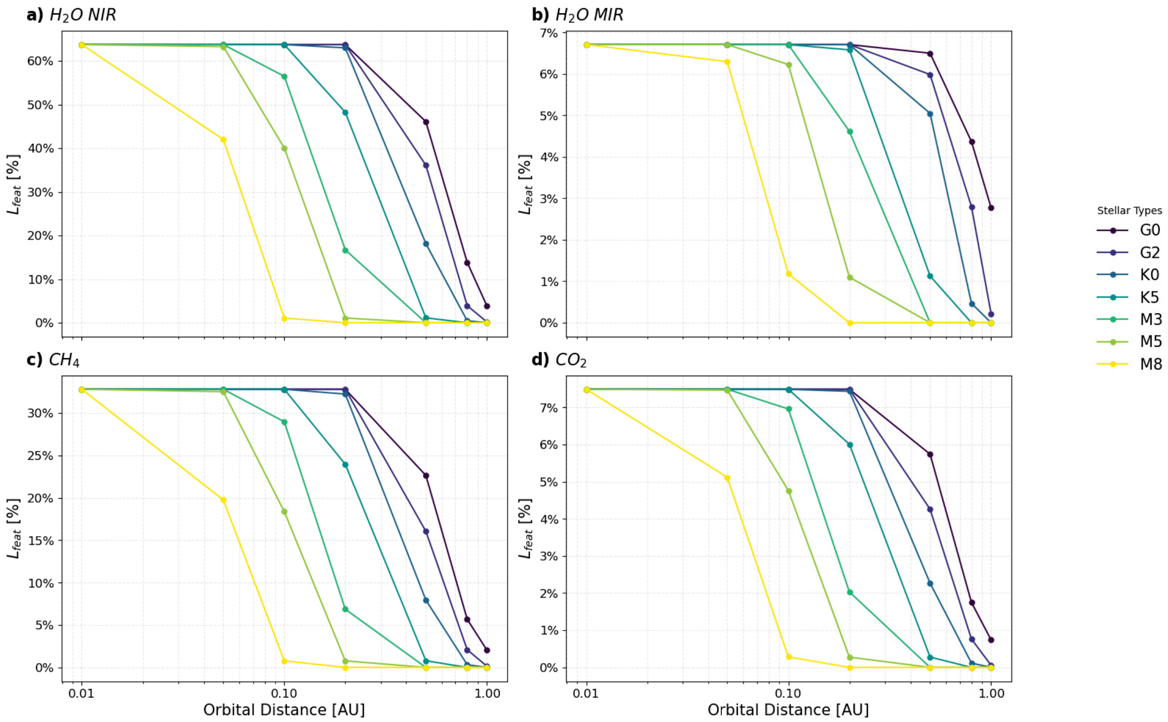

Figure 12. L_{feat} for the four analyzed spectral windows. Panels (a) H_2O NIR and (c) CH_4 show a high sensitivity to cloud masking. Panels (b) H_2O MIR and (d) CO_2 demonstrate that the features remain largely intact, with a loss of less than 10%. This illustrates the wavelength-dependent transparency of the cloud layers for the H_2O band.

4. Discussion

The comparison between the G2 and M8 systems highlights two fundamental barriers in transmission spectroscopy: the signal contrast and the refraction-limited observable atmosphere. A primary difference is immediately visible in the scaling of the transit depth. For a planet orbiting an M8 star—such as those in the TRAPPIST-1 system—the star-to-planet area ratio is significantly more favorable than for a G2 system like the Earth-Sun pair. This results in a much higher spectral contrast, which directly improves the observability and the signal-to-noise ratio for instruments like the JWST. As established in the literature, this intrinsic "astronomical" advantage makes M-dwarf planets the primary targets for the first successful characterizations of terrestrial atmospheres.

Beyond the pure signal strength, the results demonstrate how the refraction barrier acts as a "geometric" filter that changes with orbital distance. For Sun-like stars, refraction only begins to play a significant role at very large orbital distances, meaning the "refraction floor" remains deep in the atmosphere for most of the investigated range. In contrast, M8 systems show much more dynamic behavior. While the barrier is located at the surface for very close-in planets, it rises rapidly as the distance between the planet and the star increases.

At a distance of 1.0 AU, the refraction floor for an M8 system reaches nearly 0 hPa. This effectively means that the observable part of the atmosphere is pushed into layers that are located entirely above the primary cloud decks. This is where the physical limit of refraction becomes clearly visible. Because atmospheric refraction deflects light rays passing below the maximum observable pressure (p_{max}) away from the distant observer, the planet effectively appears larger, establishing a fundamental baseline for the transit depth. Consequently, the spectral contrast cannot fall below this refractive floor, causing the transmission spectra of closely orbiting G2 planets to overlap at the same continuum level. As the transmission spectrum contains no information from below this critical altitude, only gases and clouds residing above p_{max} can influence the observed spectral signatures.

Consequently, from a certain distance onward, the clouds effectively disappear from the transmission spectrum because the refracted light only probes altitudes that are physically cloud-free. In the case of M8 targets like TRAPPIST-1e, this combination of high contrast and a rising refraction barrier allows for the observation of almost the entire relevant atmosphere without being limited by refraction. This represents a decisive advantage over Earth-like planets around Sun-like stars, where atmospheric features remain dampened by astronomical and geometric parameters over a much wider range of orbital distances. This synergy between astronomical contrast and geometric transparency confirms why late M-dwarfs are the most promising laboratories for searching for molecular signatures in the future.

The comparative analysis of the clear and cloudy spectra across the entire stellar grid reveals consistent scaling trends that expand upon the initial observations of the G2 and M8 systems. When evaluating the spectra partitioned by orbital distance, the planet-to-star ratio effect becomes strikingly apparent as the contrast curves for the different stellar types are shifted relative to one another by a nearly constant factor. This shift is a direct physical representation of the stellar radius influence; as the host star becomes smaller, moving from G-type to late M-type, the relative area of the planet's atmosphere during transit increases, thus amplifying the spectral signal and confirming that higher observability is a fundamental astronomical advantage that scales predictably across the investigated stellar types.

The interplay between refraction and cloud muting dictates the physical limits of atmospheric characterization. As demonstrated, the masking effect of clouds is only relevant as long as the refraction floor allows instruments to probe deep enough to reach the cloud decks. Once the geometric barrier of refraction rises above the cloud altitude, which occurs rapidly for smaller stars at wider orbits, the observable atmosphere becomes effectively cloud-free, saturating the transmission signal at a minimum baseline.

This dynamic creates a fundamental observational paradox for planets located within the Habitable Zone (HZ). The detectability of HZ planets is strictly dictated by the opposing forces of stellar contrast and refractive geometry. For M8 dwarfs like TRAPPIST-1, the HZ is located in extreme proximity to the host star, typically between 0.02 AU and 0.06 AU (Gillon et al., 2017; Wolf et al., 2017). While these targets provide an optimal planet-to-star area ratio and exceptional spectral contrast, this tight orbital configuration keeps the refraction floor deep within the atmosphere. Consequently, instruments probe directly into the high-pressure layers where cloud decks are most prominent, allowing meteorological masking to exert its maximum influence on the transmission spectrum. In contrast, early M-type and K-type stars exhibit a more sustained sensitivity to cloud masking. For these systems, the refraction floor remains at higher pressures (deeper in the atmosphere) over a much larger range of distances, allowing clouds to mute spectral features even at wider orbits.

The G2 system represents the opposite extreme. The habitable zone for an Earth-Sun analog is estimated to lie much further out, between approximately 0.99 AU and 1.70 AU (Kopparapu et al., 2013). Over this extensive distance, the refraction floor does not rise as aggressively, meaning cloud physics theoretically remains a measurable factor. However, the absolute signal strength is so severely diluted by the massive stellar radius that any molecular features drop below the detection threshold of current instrumentation (Batalha et al., 2017).

The synergy between absolute feature amplitudes and relative spectral loss provides a comprehensive view of how clouds and refraction limit chemical characterization. While the previous global analysis established the geometric constraints, the molecular-specific data reveal a clear hierarchy in detectability based on the vertical distribution of gasses and wavelength-dependent scattering.

The most robust feature across all simulations is CO_2. In the amplitude plots, CO_2 consistently maintains the highest values and is the last molecule to show a significant decline as orbital distance increases. This is further supported by the Feature Loss data, where CO_2 exhibits the lowest relative masking. This resilience stems from the fact that CO_2 is well-mixed and remains abundant in the higher, lower-pressure layers of the atmosphere. Since its signal originates above the typical cloud deck and the rising refraction floor, it remains observable even when deeper-lying features are completely obscured.In stark contrast, CH_4 and H_2O features show a much higher sensitivity to both clouds and refraction. Because these species are more concentrated in the lower, higher-pressure regions of the atmosphere, they are the first to be muted when clouds raise the optical continuum. This truncation of the deeper atmosphere effectively closes the windows through which these molecules could be observed. As shown by the widening gap between Clear Sky and Cloudy amplitudes, the loss of information for these species is not just a reduction in peak height but a fundamental masking of their atmospheric baseline.

The results also confirm the significant role of Mie scattering in the NIR. The H_2O NIR band suffers the most severe feature loss, often exceeding 60% at close orbits. At these shorter wavelengths, the cloud particles are highly efficient at scattering light, creating a nearly opaque barrier. Moving into the Mid-Infrared (MIR), however, the effectiveness of Mie scattering diminishes. The H_2O MIR and CH_4 features remain much more accessible. This transition from NIR-opaque to MIR-transparent regimes—predicted in the methodological hypothesis—is clearly evidenced by the significantly lower feature loss in the MIR panels. For observers, this implies that while water vapor might appear to be missing or heavily depleted in NIR observations (e.g., with JWST/NIRSpec), MIR observations (e.g., with JWST/MIRI) can still retrieve these signatures by probing through the partially transparent cloud deck.

Ultimately, this leaves early M-type and K-type stars as a compelling geometric middle ground for transmission spectroscopy. For these systems, the refraction floor remains low enough to probe the lower atmosphere over a larger range of orbital distances, while the stellar radii still provide a more manageable astronomical contrast. Although the refractive floor for G-type stars at wider orbits rises high enough to obscure the primary, dense cloud decks, the feature loss (L_{feat}) never completely reaches zero (as seen in Figure 12). Since the instrument model utilized in this study assumes an idealized setup without noise, these minute deviations are not statistical artifacts. Instead, they represent a genuine physical signal caused by optically thin, high-altitude ice clouds and residual water vapor protruding above the maximum observable pressure (p_{max}). However, it is crucial to place this residual muting effect into a realistic observational context. The absolute signal difference caused by these high-altitude clouds in G-star systems is well below 1 ppm. In reality, this signal would be completely indistinguishable from actual observational noise, as it falls orders of magnitude below the expected systematic

noise floors of JWST instruments, which are currently estimated to be around 20 to 50 ppm (Greene et al., 2016; Suissa et al., 2020).
However, as demonstrated by Suissa et al., 2020, exploiting this geometric advantage remains observationally challenging. The results indicate that the reduced planet-to-star radius ratio for mid-K and early-M dwarfs results in spectral features that often fall below 1 ppm, rendering JWST transmission spectroscopy exceedingly difficult. To fully characterize these targets, comprehensive spectral coverage is essential.

5. Conclusion

In summary, the presence of clouds significantly reshapes the detectability of molecular features, acting as a competitive source of opacity alongside the geometric constraint of refraction. Returning to the central research question, the influence of clouds is maximized when the planet-to-star radius ratio is high and the orbital distance is small. Late-type stars, such as M-dwarfs, provide the most favorable contrast for detecting atmospheric signals. However, these systems also exhibit the most dramatic susceptibility to cloud masking at close orbits. At these proximities, the refraction floor is situated deep in the atmosphere, allowing the instrument to probe the high-pressure layers where cloud decks are most prominent. Consequently, the transit depth is maximized, but so too is the relative signal loss—often exceeding 20%—as clouds raise the optical continuum and truncate the minima in the transit spectra. Ultimately, while small stars offer the best observational window in terms of SNR, they also force a confrontation with the most severe cloud effects, particularly within their habitable zones. Conversely, while larger G-type stars minimize the relative impact of clouds over greater distances, the inherent lack of contrast renders these cloud-muted signatures nearly undetectable with current technology.

Building upon the geometric and meteorological constraints established in this work, a logical next step is to incorporate comprehensive instrumental noise models to evaluate these findings under realistic observing conditions. Quantifying the exact number of transits required to achieve robust detection of these specific molecules will be the final crucial step in translating theoretical observability into practically possible JWST observations.

Bibliography

Alp, D., & Demory, B.-O. (2018). Refraction in exoplanet atmospheres - Photometric signatures, implications for transmission spectroscopy, and search in Kepler data. *Astronomy & Astrophysics*, *609*, A90. https://doi.org/10.1051/0004-6361/201731484

Barstow, J. K., Aigrain, S., Irwin, P. G. J., Kendrew, S., & Fletcher, L. N. (2015). Transit spectroscopy with James Webb Space Telescope: Systematics, starspots and stitching. *Monthly Notices of the Royal Astronomical Society*, *448*(3), 2546–2561. https://doi.org/10.1093/mnras/stv186

Batalha, N. E., Mandell, A., Pontoppidan, K., Stevenson, K. B., Lewis, N. K., Kalirai, J., Earl, N., Greene, T., Albert, L., & Nielsen, L. D. (2017). PandExo: A Community Tool for Transiting Exoplanet Science with JWST & HST. *Publications of the Astronomical Society of the Pacific*, *129*(976), 064501. https://doi.org/10.1088/1538-3873/aa65b0

Beichman, C., Benneke, B., Knutson, H., Smith, R., Lagage, P.-O., Dressing, C., Latham, D., Lunine, J., Birkmann, S., Ferruit, P., Giardino, G., Kempton, E., Carey, S., Krick, J., Deroo, P. D., Mandell, A., Ressler, M. E., Shporer, A., Swain, M., ... Sing, D. (2014). Observations of Transiting Exoplanets with the James Webb Space Telescope (*JWST*). *Publications of the Astronomical Society of the Pacific*, *126*(946), 1134–1173. https://doi.org/10.1086/679566

Betremieux, Y., & Kaltenegger, L. (2014). Impact of atmospheric refraction: How deeply can we probe exo-Earth's atmospheres during primary eclipse observations? [arXiv:1312.6625 [astro-ph]]. *The Astrophysical Journal*, *791*(1), 7. https://doi.org/10.1088/0004-637X/791/1/7

Brown, T. M. (2001). Transmission Spectra as Diagnostics of Extrasolar Giant PlanetAtmospheres. *The Astrophysical Journal*, *553*(2), 1006. https://doi.org/10.1086/320950

Charbonneau, D., Brown, T. M., Latham, D. W., & Mayor, M. (1999). Detection of Planetary Transits Across a Sun-likeStar. *The Astrophysical Journal*, *529*(1), L45. https://doi.org/10.1086/312457

Christiansen, J. L., McElroy, D. L., Harbut, M., Ciardi, D. R., Crane, M., Good, J., Hardegree-Ullman, K. K., Kesseli, A. Y., Lund, M. B., Lynn, M., Muthiar, A., Nilsson, R., Oluyide, T., Papin, M., Rivera, A., Swain, M., Susemiehl, N. D., Tam, R., Eyken, J. v., & Beichman, C. (2025). The NASA Exoplanet Archive and Exoplanet Follow-up Observing Program: Data, Tools, and Usage. *The Planetary Science Journal*, *6*(8), 186. https://doi.org/10.3847/PSJ/ade3c2

Cowan, N. B., Greene, T., Angerhausen, D., Batalha, N. E., Clampin, M., Colon, K., Crossfield, I. J. M., Fortney, J. J., Gaudi, B. S., Harrington, J., Iro, N., Lillie, C. F., Linsky, J. L., Lopez-Morales, M., Mandell, A. M., & Stevenson, K. B. (2015). Characterizing Transiting Planet Atmospheres through 2025 [arXiv:1502.00004 [astro-ph]]. *Publications of the Astronomical Society of the Pacific*, *127*(949), 311–327. https://doi.org/10.1086/680855

Doshi, D., Cowan, N. B., & Huang, Y. (2022). Stratospheric clouds do not impede JWST transit spectroscopy for exoplanets with Earth-like atmospheres. *Monthly Notices of the Royal Astronomical Society*, *515*(2), 1982–1992. https://doi.org/10.1093/mnras/stac1869

Fauchez, T. J., Turbet, M., Villanueva, G. L., Wolf, E. T., Arney, G., Kopparapu, R. K., Lincowski, A., Mandell, A., Wit, J. d., Pidhorodetska, D., Domagal-Goldman, S. D., & Stevenson, K. B. (2019). Impact of Clouds and Hazes on the Simulated JWST Transmission Spectra of Habitable Zone Planets in the TRAPPIST-1 System. *The Astrophysical Journal*, *887*(2), 194. https://doi.org/10.3847/1538-4357/ab5862

Fauchez, T. J., Turbet, M., Wolf, E. T., Boutle, I., Way, M. J., Del Genio, A. D., Mayne, N. J., Tsigaridis, K., Kopparapu, R. K., Yang, J., Forget, F., Mandell, A., & Domagal Goldman, S. D. (2020). TRAPPIST-1 Habitable Atmosphere Intercomparison (THAI): Motivations and protocol version 1.0. *Geoscientific Model Development*, *13*(2), 707–716. https://doi.org/10.5194/gmd-13-707-2020

Fauchez, T. J., Villanueva, G. L., Sergeev, D. E., Turbet, M., Boutle, I. A., Tsigaridis, K., Way, M. J., Wolf, E. T., Domagal-Goldman, S. D., Forget, F., Haqq-Misra, J., Kopparapu, R. K., Manners, J., & Mayne, N. J. (2022). The TRAPPIST-1 Habitable Atmosphere Intercomparison (THAI). III. Simulated Observables—the Return of the Spectrum. *The Planetary Science Journal*, *3*(9), 213. https://doi.org/10.3847/PSJ/ac6cf1

Gardner, J. P., Mather, J. C., Clampin, M., Doyon, R., Greenhouse, M. A., Hammel, H. B., Hutchings, J. B., Jakobsen, P., Lilly, S. J., Long, K. S., Lunine, J. I., Mccaughrean, M. J., Mountain, M., Nella, J., Rieke, G. H., Rieke, M. J., Rix, H.-W., Smith, E. P., Sonneborn, G., … Wright, G. S. (2006). The James Webb Space Telescope. *Space Science Reviews*, *123*(4), 485–606. https://doi.org/10.1007/s11214-006-8315-7

Gates, W. L. (1992). AN AMS CONTINUING SERIES: GLOBAL CHANGE–AMIP: The Atmospheric Model Intercomparison Project. *Bulletin of the American Meteorological Society*, *73*(12), 1962–1970. https://doi.org/10.1175/1520-0477(1992)073<1962:ATAMIP>2.0.CO;2

Gillon, M., Triaud, A. H. M. J., Demory, B.-O., Jehin, E., Agol, E., Deck, K. M., Lederer, S. M., de Wit, J., Burdanov, A., Ingalls, J. G., Bolmont, E., Leconte, J., Raymond, S. N., Selsis, F., Turbet, M., Barkaoui, K., Burgasser, A., Burleigh, M. R., Carey, S. J., … Queloz, D. (2017). Seven temperate terrestrial planets around the nearby ultracool dwarf star TRAPPIST-1. *Nature*, *542*(7642), 456–460. https://doi.org/10.1038/nature21360

Giorgetta, M. A., Brokopf, R., Crueger, T., Esch, M., Fiedler, S., Helmert, J., Hohenegger, C., Kornblueh, L., Köhler, M., Manzini, E., Mauritsen, T., Nam, C., Raddatz, T., Rast, S., Reinert, D., Sakradzija, M., Schmidt, H., Schneck, R., Schnur, R., … Stevens, B. (2018). ICON-A, the Atmosphere Component of the ICON Earth System Model: I. Model Description. *Journal of Advances in Modeling Earth Systems*, *10*(7), 1613–1637. https://doi.org/10.1029/2017MS001242

Gordon, I. E., Rothman, L. S., Hargreaves, R. J., Hashemi, R., Karlovets, E. V., Skinner, F. M., Conway, E. K., Hill, C., Kochanov, R. V., Tan, Y., Wcisło, P., Finenko, A. A., Nelson, K., Bernath, P. F., Birk, M., Boudon, V., Campargue, A., Chance, K. V., Coustenis, A., … Yurchenko, S. N. (2022). The HITRAN2020 molecular spectroscopic database. *Journal of Quantitative Spectroscopy and Radiative Transfer*, *277*, 107949. https://doi.org/10.1016/j.jqsrt.2021.107949

Gould, A., Pepper, J., & DePoy, D. L. (2003). Sensitivity of Transit Searches to Habitable Planets [arXiv:astro-ph/0211547]. *The Astrophysical Journal*, *594*(1), 533–537. https://doi.org/10.1086/376852

Greene, T. P., Line, M. R., Montero, C., Fortney, J. J., Lustig-Yaeger, J., & Luther, K. (2016). CHARACTERIZING TRANSITING EXOPLANET ATMOSPHERES WITH JWST. *The Astrophysical Journal*, *817*(1), 17. https://doi.org/10.3847/0004-637X/817/1/17

Komacek, T. D., Fauchez, T. J., Wolf, E. T., & Abbot, D. S. (2020). Clouds will Likely Prevent the Detection of Water Vapor in JWST Transmission Spectra of Terrestrial Exoplanets. *The Astrophysical Journal Letters*, *888*(2), L20. https://doi.org/10.3847/2041-8213/ab6200

Kopparapu, R. K., Ramirez, R., Kasting, J. F., Eymet, V., Robinson, T. D., Mahadevan, S., Terrien, R. C., Domagal-Goldman, S., Meadows, V., & Deshpande, R. (2013). HABITABLE ZONES AROUND MAIN-SEQUENCE STARS: NEW ESTIMATES. *The Astrophysical Journal*, *765*(2), 131. https://doi.org/10.1088/0004-637X/765/2/131

Kreidberg, L. (2017). Exoplanet Atmosphere Measurements from Transmission Spectroscopy and Other Planet Star Combined Light Observations. In H. J. Deeg & J. A. Belmonte (Eds.), *Handbook of Exoplanets* (pp. 1–23). Springer International Publishing. https://doi.org/10.1007/978-3-319-30648-3_100-1

Lustig-Yaeger, J., Meadows, V. S., Crisp, D., Line, M. R., & Robinson, T. D. (2023). Earth as a Transiting Exoplanet: A Validation of Transmission Spectroscopy and Atmospheric Retrieval Methodologies for Terrestrial Exoplanets. *The Planetary Science Journal*, *4*(9), 170. https://doi.org/10.3847/PSJ/acf3e5

Lustig-Yaeger, J., Meadows, V. S., & Lincowski, A. P. (2019). The Detectability and Characterization of the TRAPPIST-1 Exoplanet Atmospheres with JWST. *The Astronomical Journal*, *158*(1), 27. https://doi.org/10.3847/1538-3881/ab21e0

Macdonald, E. J. R., & Cowan, N. B. (2019). An empirical infrared transit spectrum of Earth: Opacity windows and biosignatures. *Monthly Notices of the Royal Astronomical Society*, *489*(1), 196–204. https://doi.org/10.1093/mnras/stz2047

Misra, A., Meadows, V., & Crisp, D. (2014). The Effects of Refraction on Transit Transmission Spectroscopy: Application to Earth-like Exoplanets [arXiv:1407.3265 [astro-ph]]. *The Astrophysical Journal*, *792*(1), 61. https://doi.org/10.1088/0004-637X/792/1/61

Moran, S. E., Hörst, S. M., Batalha, N. E., Lewis, N. K., & Wakeford, H. R. (2018). Limits on Clouds and Hazes for the TRAPPIST-1 Planets. *The Astronomical Journal*, *156*(6), 252. https://doi.org/10.3847/1538-3881/aae83a

NASA, P. S. G. (2025, April). Nasapsg/globes [original-date: 2021-02-26T18:19:02Z]. Retrieved May 4, 2026, from https://github.com/nasapsg/globes

Nutzman, P., & Charbonneau, D. (2008). Design Considerations for a Ground-Based Transit Search for Habitable Planets Orbiting M Dwarfs. *Publications of the Astronomical Society of the Pacific*, *120*(865), 317. https://doi.org/10.1086/533420

Pidhorodetska, D., Fauchez, T. J., Villanueva, G. L., Domagal-Goldman, S. D., & Kopparapu, R. K. (2020). Detectability of Molecular Signatures on TRAPPIST-1e through Transmission Spectroscopy Simulated for Future Space-based Observatories. *The Astrophysical Journal Letters*, *898*(2), L33. https://doi.org/10.3847/2041-8213/aba4a1

Robinson, T. D. (2005). Earth as an Exoplanet. In *Planetary Astrobiology* (pp. 1–1). University of Arizona Press. https://doi.org/10.2458/azu_uapress_9780816540068-ch015

Seager, S., & Sasselov, D. D. (2000). Theoretical Transmission Spectra During Extrasolar Giant Planet Transits [arXiv:astro-ph/9912241]. *The Astrophysical Journal*, *537*(2), 916–921. https://doi.org/10.1086/309088

Seager, S., & Deming, D. (2010). Exoplanet Atmospheres. *Annual Review of Astronomy and Astrophysics*, *48*(Volume 48, 2010), 631–672. https://doi.org/10.1146/annurev-astro-081309-130837

Seager, S., & Mallen-Ornelas, G. (2003). On the Unique Solution of Planet and Star Parameters from an Extrasolar Planet Transit Light Curve [arXiv:astro-ph/0206228]. *The Astrophysical Journal*, *585*(2), 1038–1055. https://doi.org/10.1086/346105

Sergeev, D. E., Fauchez, T. J., Turbet, M., Boutle, I. A., Tsigaridis, K., Way, M. J., Wolf, E. T., Domagal-Goldman, S. D., Forget, F., Haqq-Misra, J., Kopparapu, R. K., Lambert, F. H., Manners, J., & Mayne, N. J. (2022). The TRAPPIST-1 Habitable Atmosphere Intercomparison (THAI). II. Moist Cases—The Two Waterworlds. *The Planetary Science Journal*, *3*(9), 212. https://doi.org/10.3847/PSJ/ac6cf2

Shields, A. L., Ballard, S., & Johnson, J. A. (2016). The Habitability of Planets Orbiting M-dwarf Stars [arXiv:1610.05765 [astro-ph]]. *Physics Reports*, *663*, 1–38. https://doi.org/10.1016/j.physrep.2016.10.003

Sidis, O., & Sari, R. (2010, August). Transits of Transparent Planets - Atmospheric Lensing Effects [arXiv:1008.0643 [astro-ph]]. https://doi.org/10.48550/arXiv.1008.0643

Suissa, G., Mandell, A. M., Wolf, E. T., Villanueva, G. L., Fauchez, T., & Kopparapu, R. k. (2020). Dim Prospects for Transmission Spectra of Ocean Earths around M Stars. *The Astrophysical Journal*, *891*(1), 58. https://doi.org/10.3847/1538-4357/ab72f9

Villanueva, G. L., Liuzzi, G., Faggi, S., Protopapa, S., Kofman, V., Fauchez, T., Stone, S. W., & Mandell, A. M. (2022). *Fundamentals of the Planetary Spectrum Generator*. https://ui.adsabs.harvard.edu/abs/2022fpsg.book.....V

Wolf, E. T., Shields, A. L., Kopparapu, R. K., Haqq-Misra, J., & Toon, O. B. (2017). Constraints on Climate and Habitability for Earth-like Exoplanets Determined from a General Circulation Model. *The Astrophysical Journal*, *837*(2), 107. https://doi.org/10.3847/1538-4357/aa5ffc

Wunderlich, F., Godolt, M., Grenfell, J. L., Städt, S., Smith, A. M. S., Gebauer, S., Schreier, F., Hedelt, P., & Rauer, H. (2019). Detectability of atmospheric features of Earth-like planets in the habitable zone around M dwarfs. *Astronomy & Astrophysics*, *624*, A49. https://doi.org/10.1051/0004-6361/201834504

A. Appendix

This appendix provides supplementary material and data that support the primary analysis presented in this study. Figure 13 illustrates the differences between the cloudy and clear-sky scenarios across the entire range of simulated orbital distances. This visualization highlights the raw magnitude of the transit signal lost to cloud opacity. Additionally, the specific configuration parameters and atmospheric profiles utilized for the PSG simulations are documented in Table 2.

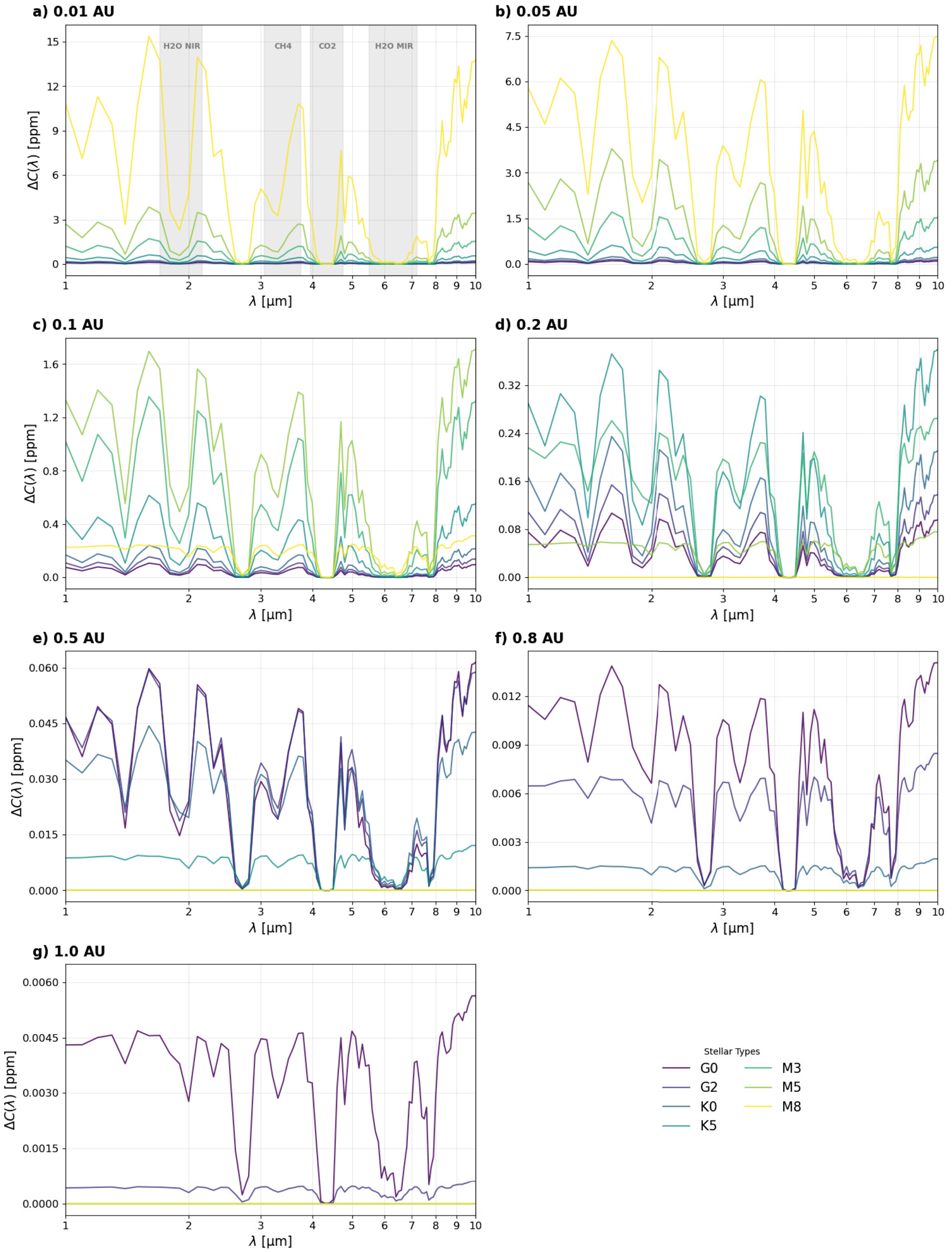

Figure 13. Spectral difference ($\Delta C(\lambda)$) as a function of star-planet distance. Each panel displays the absolutely "lost" transit signal, calculated as the difference between the clear-sky and cloudy contrast ($C_{clear} - C_{cloudy}$). Results are shown for orbital distances from (a) 0.01 AU to (g) 1 AU.

Variable	Value	Description
<OBJECT-NAME>	Earth	Name of the planet
<OBJECT-DIAMETER>	12742	Equatorial diameter in km
<OBJECT-GRAVITY>	9.81	Surface gravity in m/s^2
<OBJECT-GRAVITY-UNIT>	g	Gravity unit
<OBJECT-STAR-DISTANCE>	**0.10**	Distance to the star in AU (varied)
<OBJECT-STAR-TYPE>	**M8**	Spectral type of the star (varied)
<OBJECT-STAR-TEMPERATURE>	**3000**	Effective temperature of the star in K (varied)
<OBJECT-OBS-LONGITUDE>	180.0	Sub-observer longitude
<OBJECT-OBS-LATITUDE>	0.0	Sub-observer latitude
<OBJECT-PERIOD>	365	Orbital period in days
<GEOMETRY>	Observatory	Viewing geometry (space telescope)
<GEOMETRY-OBS-ALTITUDE>	1.0	Distance from observer to planet in parsecs
<GEOMETRY-PLANET-FRACTION>	1.0	Fraction of the planetary disk being observed
<ATMOSPHERE-WEIGHT>	28.97	Mean molecular weight of the atmosphere
<ATMOSPHERE-DESCRIPTION>	ICON	GCM model name
<ATMOSPHERE-PRESSURE>	1	Surface pressure in bar
<ATMOSPHERE-STRUCTURE>	Equilibrium	Type of atmospheric structure; here: hydrostatic equilibrium
<ATMOSPHERE-GAS>	N2, O2, CO2, ...	List of gases in the atmosphere
<ATMOSPHERE-TYPE>	HIT[...]	Data source for gas absorption
<ATMOSPHERE-ABUN>	78, 20.9, ...	Gas abundances in percentage or ppm
<ATMOSPHERE-AEROS>	WaterIce, Water	Aerosol/cloud types
<ATMOSPHERE-ASIZE>	30,10	effective radius of aerosols
<ATMOSPHERE-ATYPE>	Warren_ice_HRI, ...	Optical properties of aerosols
<ATMOSPHERE-NMAX>	20	scattering calculations
<ATMOSPHERE-LMAX>	80	scattering calculations
ATMOSPHERE-CLOUDFRACTION	eg. 1	fraction of the planet covered with clouds
<GENERATOR-RANGE1>	0.5	Start of wavelength range (µm)
<GENERATOR-RANGE2>	30.0	End of wavelength range (µm)
<GENERATOR-RESOLUTION>	0.1	Spectral resolution (µm)
<GENERATOR-RESOLUTIONUNIT>	um	unit of resolution
<GENERATOR-NOISE>	N	No noise model used
<GENERATOR-TRANS-APPLY>	Y	Enable transit simulation
<GENERATOR-TRANS-SHOW>	N	Disable plotting extra transit views
<GENERATOR-GAS-MODEL>	Y	Enable gas absorption modeling
<GENERATOR-CONT-MODEL>	Y	Enable continuum modeling
<GENERATOR-LOGRAD>	N	Do not use logarithmic radiance

Table 2. Configuration parameters used for PSG simulations (Villanueva et al., 2022). The bold values indicate parameters that are varied during the parameter study.